



UNIVERSITÉ DE GENÈVE

FACULTY OF SCIENCE

Stopping Proton Studies

For the SuperFGD Prototype

THESIS MSc NUCLEAR AND PARTICLE PHYSICS

Author:

Dana DOUQA

Supervisor:

Prof. Federico SANCHEZ NIETO

September 9, 2019

Abstract

The SuperFine-Grained Detector (SuperFGD) is an integral component of the upgraded ND280 detector in the T2K experiment. In the summer of 2018, a beam test was performed on a prototype of the SuperFGD at CERN. The test was then followed by a series of studies carried out by the beam test analysis group, one of which was the subject of this thesis.

This study aims to isolate a sample of stopping protons using careful event selection criteria. The sample is then analyzed to extract some of the characteristics of stopping protons, such as their range in the detector and their dE/dx curve.

In parallel, simulations of the SuperFGD prototype were used for reference and to perform some comparisons with the beam test data. These comparisons shed light on some effects that need to be taken into account in the simulation of the detector response. The analysis was concluded with an investigation of the effects of simulating the cube coating and the fibers of the SuperFGD as dead volume in the detector.

Acknowledgements

This has been a wonderful project for me to join at a perfect time and I deeply appreciate that. Especially for a student at my level, it was a great experience to witness the assembly of the detector, be part of the beam test, and then actively work on the data.

My deep gratitude goes first to professor Federico Sanchez for giving me this great opportunity and providing constant guidance and feedback throughout this study. I am also truly thankful for encouraging me to take part in the project meetings and present my results in front of the ND280 upgrade collaboration.

I am very thankful to Etam Noah for leading the beam test analysis group, providing his valuable input in every step of this work, and for trusting me to do important tasks from the very beginning. I am also especially thankful to Saba Parsa for her big role in helping me integrate in the project when I first started and answering all my questions along the way. I would also like to thank the ND280 upgrade simulation group for their help in using the simulations and troubleshooting some issues I faced.

Furthermore, I would like to give special thanks to the Faculty of Science of the University of Geneva for granting me the Excellence Master Fellowship, without which my studies may not have been possible.

Finally, I wish to express very special gratitude to my family for all their support throughout my life, and especially the last two years. Thank you for believing in me and I hope I always make you proud.

And Anas, thank you for being my rock and cornerstone.

Till the sun freezes and the moon dies.

Disclaimer

The majority of this work was performed during the end of 2018/beginning of 2019 and is based on the ND280 Upgrade Technical Design Report (Jan 2019). Since the ND280 upgrade is a project that is in progress, some specifications mentioned in this thesis may have been altered based on decisions made thereafter.

Contents

1. Introduction	1
2. The T2K Experiment	2
2.1. The Experiment	2
2.2. The Current Near Detector	3
2.2.1. The Pi-0 Detector (P0D)	4
2.2.2. The Time-Projection Chambers (TPCs)	5
2.2.3. The Fine-Grained Detectors (FGDs)	6
2.2.4. The Electromagnetic Calorimeters (ECal)	7
2.2.5. The UA1 Magnet	7
2.2.6. The Side Muon-Range Detector (SMRD)	8
2.3. Neutrino Detection in the ND280	9
2.4. The ND280 Upgrade	10
2.4.1. Motivation for Upgrade	10
2.4.2. The Upgraded ND280 Design	11
3. Scintillator Detectors	14
3.1. Concept	14
3.2. Proton Interactions in Matter	16
3.3. Birk's Law	17
4. The SuperFGD	19
4.1. The Scintillating Cubes	20
4.2. Wavelength-Shifting Fibers	20
4.3. Multi-Pixel Photon Counters	23
4.4. The Mechanical Box	27
4.5. The Readout Electronics	28
4.6. The SuperFGD Prototype	31
4.6.1. Assembly	31
4.6.2. Prototype Electronics	32
4.6.3. Data Acquisition (DAQ) and Recorded Data	33
4.6.4. Data Structure	36
4.6.5. Calibration	36

5. The Beam Test	40
5.1. The T9 Beam Environment	40
5.2. Test Setup	41
6. Simulation of the SuperFGD	43
6.1. Simulation of the Detector Geometry	44
6.2. Simulation of the Detector Response	44
6.3. Creating Simulations for the SuperFGD Prototype	45
7. Stopping Proton Studies	46
7.1. Motivation to Study Stopping Protons	47
7.2. Samples of Stopping Protons	47
7.2.1. Beam Test Data and Data Quality	47
7.2.2. SuperFGD Proton Beam Simulations	48
7.2.3. Event Selection	49
7.3. Event Displays	52
7.4. Part 1: Selection of Simulation Sample	53
7.4.1. The Range of Protons in the SuperFGD	53
7.4.2. Beam Momentum Analysis	58
7.5. Part 2: Beam Test Data vs. Simulation Analysis	62
7.5.1. Obtaining the dE/dz Curves	62
7.5.2. dE/dz Comparison	64
7.5.3. Fiber Response Comparison	68
7.5.3.1. Attenuation	68
7.5.3.2. Energy Deposition	69
7.6. Effect of Cube Coating, Holes and Fibers(From Simulations)	72
8. Conclusion	75
Bibliography	76
A. Calculation of Uncertainties	78
A.1. Uncertainty in the Reconstructed Momentum	78
A.2. Uncertainty in the Kinetic Energy From The Range	78
B. Samples of Event Displays	80
B.1. 800 MeV/c Beam Test Sample	80
B.2. 750 MeV/c Simulation Sample	83

*Stands at the sea,
wonders at wondering: I
a universe of atoms
an atom in the universe.*

— Richard Feynman

1

Introduction

The T2K experiment is a long baseline neutrino experiment in Japan. In 2017 a project was launched to upgrade one of the experiment's near detectors, the ND280. The new design for the ND280 includes a highly granular scintillator detector based on a novel idea to use $1 \times 1 \times 1 \text{ cm}^3$ cubes read out along three orthogonal directions by wavelength-shifting fibers. This detector, named the SuperFine-Grained Detector (SuperFGD), is the subject of this study.

In the summer of 2018, a beam test was performed on a prototype of the SuperFGD using the T9 beam at CERN. This study is one of many studies that were conducted in order to characterize the performance and response of the SuperFGD prototype.

Following this introduction, chapter 2 briefly describes the T2K experiment in general, the current ND280 and its upgrade plans. Chapter 3 provides some information on scintillator detectors, followed by chapter 4 which describes the SuperFGD in detail. The beam test and setup are then described in chapter 5.

The ND280 upgrade simulation group has created simulations for the SuperFGD which can be adapted for the prototype. These simulations were used in this study and compared against the beam test data. Chapter 6 describes the creation of these simulations and how some aspects of the detector response were introduced.

Chapter 7 is the analysis part where the event selection procedure used to obtain the stopping protons sample is explained in detail. In this chapter, results are presented for both beam test data and simulations. These results are then compared and the conclusions are summarized in chapter 8.

*The good thing about science is that it is true,
whether you believe in it or not.*

— Neil deGrasse Tyson

2

The T2K Experiment

Contents

2.1. The Experiment	2
2.2. The Current Near Detector	3
2.2.1. The Pi-0 Detector (P0D)	4
2.2.2. The Time-Projection Chambers (TPCs)	5
2.2.3. The Fine-Grained Detectors (FGDs)	6
2.2.4. The Electromagnetic Calorimeters (ECal)	7
2.2.5. The UA1 Magnet	7
2.2.6. The Side Muon-Range Detector (SMRD)	8
2.3. Neutrino Detection in the ND280	9
2.4. The ND280 Upgrade	10
2.4.1. Motivation for Upgrade	10
2.4.2. The Upgraded ND280 Design	11

2.1. The Experiment

The T2K (Tokai-to-Kamioka) experiment is a long-baseline neutrino experiment in Japan studying neutrino oscillations. A muon-neutrino beam is generated at the J-PARC accelerator in Tokai and sent 295 km to the far detector, Super-Kamiokande, in Kamioka.

To create a neutrino beam, a proton beam collides with a graphite target producing pions which are focused by a system of two magnetic horns. Focused pions travel through a decay tunnel producing muons and muon neutrinos.

A second layer of graphite is then used to stop muons and the remaining protons that did not interact with the target, allowing only neutrinos to pass. The T2K beam line is shown in figure 2.1.

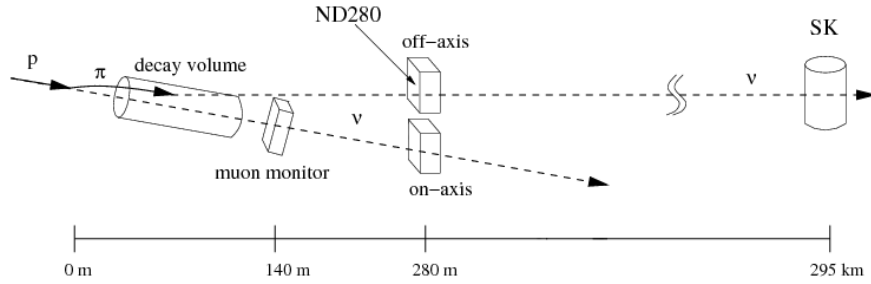


Figure 2.1.: The T2K neutrino beam line^[11].

The T2K neutrino beam has a broad energy spectrum with a prominent flux peak around 600 MeV. This energy is carefully chosen such that neutrinos would have a high probability of undergoing oscillations after travelling 295 km. In order to select a narrower range of energies, neutrino oscillations are studied utilizing the off-axis part of the beam. Therefore, the ND280 and Super-Kamiokande are both placed 2.5 degrees off of the beam center^[1]. T2K is the first off-axis long-baseline neutrino experiment.

2.2. The Current Near Detector

For the purpose of detecting and measuring neutrinos before oscillations, a set of neutrino detectors is placed at a distance of 280 m from the target. The on-axis Interactive Neutrino GRID (INGRID) near detector measures the direction and intensity of the beam by studying neutrino interactions in iron. This check is performed in order to ensure that the stability of the direction of the beam is within 1/20th of a degree and that the intensity is constant over time.

The off-axis near detector ND280 is placed 2.5 degrees away from the centre of the neutrino beam and is used to measure the flux, flavor content and energy spectrum of the neutrino beam, and study neutrino-nucleus interactions. It consists of a Pi-Zero detector (POD), an electromagnetic calorimeter (ECal), three Time Projection Chambers (TPCs), two Fine-Grained Detectors (FGDs), and a side muon range detector (SMRD). All detectors are enclosed within the UA1 magnet operating at 0.2 T.

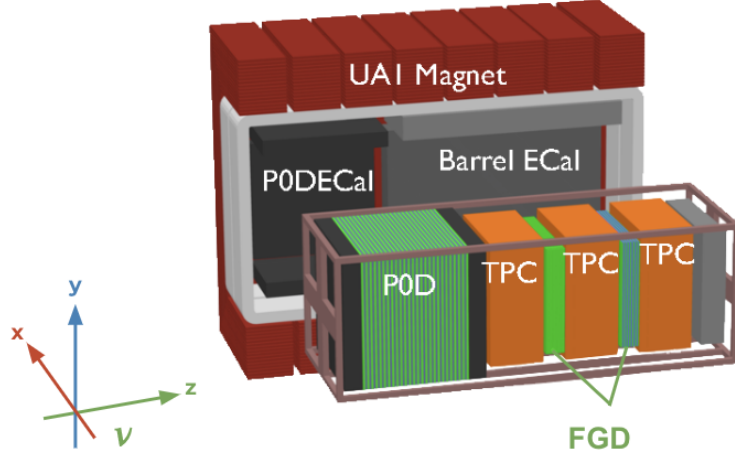


Figure 2.2.: The current ND280 detector.

2.2.1. The Pi-0 Detector (P0D)

The P0D is the most upstream detector in the ND280. It consists of two electromagnetic calorimeters (upstream and downstream in the direction of the neutrino beam) surrounding the target region.

The target region of the P0D is composed of alternating layers of water and plastic scintillators, with sheets of brass between them to decrease the average radiation length of the detector.

The P0D specializes in measuring the inclusive π^0 production when muon neutrinos interact with oxygen

$$\nu_\mu + n(p) \rightarrow \nu_\mu + n(p) + \pi^0 \quad (2.1)$$

Measurement of the cross section of this process is important since the decay of a π^0 to two photons, which in turn create electron/positron pairs, constitutes the main background to the production of an electron from an electron neutrino. The latest being the process by which the appearance of electron neutrinos is observed.

$$\nu_e + N \rightarrow e^- + X \quad (2.2)$$

In other words, the P0D must have a high efficiency in detecting photons. Therefore, the sheets of brass are used in order to increase the probability of the photons to produce e^-e^+ pairs in the central region of the detector.

2.2.2. The Time-Projection Chambers (TPCs)

Three time-projection chambers are placed in the ND280 directly after the P0D and each of the FGDs to detect and track any charged particles that emerge from the FGDs. The TPC uses a low diffusion gas to obtain a momentum resolution of $\leq 10\%$ for particles below 1 GeV/c with a 0.2 T magnetic field^[11]. With this resolution, the momentum and charge of the particle can be reconstructed from its curvature in the magnetic field.

TPCs also play a significant role in particle identification using dE/dx curves to separate muons from electrons, as seen in figure 2.3.

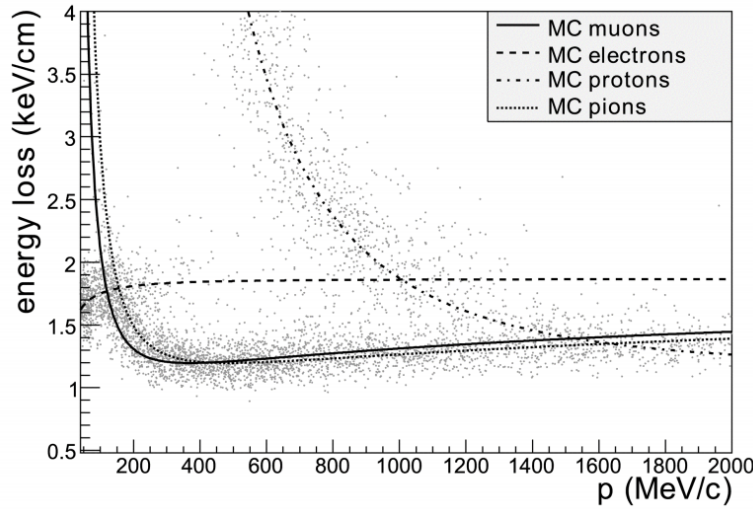


Figure 2.3.: dE/dx of positively charged particles as a function of their momentum, measured by a single TPC during the first T2K physics run. The curves represent the expected values for muons, positrons, protons, and pions^[1].

For the 600 MeV/c T2K beam, the difference in dE/dx between the electrons and the muons is of the order of 30%-40%. Consequently, muons and electrons can be separately identified by the TPC with a 3σ identification provided that the resolution of dE/dx in the TPC is better than 10%^[12].

The TPCs of the ND280 are rectangular boxes with a cathode in the center between two drift chambers that are filled with an Argon-based gas. 12 MicroMegas^[13] modules are placed on each of the lateral sides of the detector to provide the readout electronics, each of which provides a grid of 48×36 pads. Figure 2.4 shows the design of the T2K TPCs.

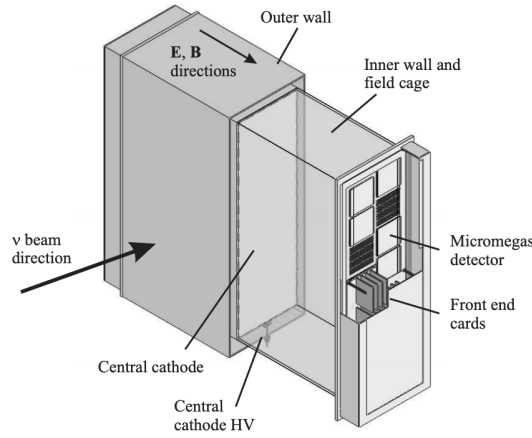


Figure 2.4.: The T2K TPC^[11].

2.2.3. The Fine-Grained Detectors (FGDs)

The two fine-grained detectors in the ND280 provide an essential target mass for neutrino interactions. The upstream FGD1 is positioned directly after the first TPC and consists of 30 layers of extruded scintillator bars that alternate in vertical and horizontal orientations in the plane perpendicular to the beam. On the other hand, FGD2 is made of six 3 cm thick layers of water sandwiched between 7 scintillator layers. Together, they have a mass of 2.0 tons.

The FGDs are made to be thin enough such that most of the particles produced by neutrino interactions would reach the TPCs where their charge and momenta are measured using their curvature in the 0.2 T magnetic field. On the other hand, short-ranged particles around the interaction vertex are tracked in the FGDs which requires them to have a fine granularity^[4]. To achieve the necessary fine granularity, the bars have a square cross section with a side of 9.6 mm.

Figure 2.5 shows a cross-sectional view of an FGD. Each XY module consists of a layer of 192 bars oriented along the X direction, glued to a layer of 192 bars along the Y direction. A support strap of 0.25 mm thickness is used between the modules to provide additional mechanical rigidity. The signal from the scintillator bars is transferred via wavelength-shifting fibers to a Multi-Pixel Photon Counter (MPPC) at one end of the fiber for readout. The detector is surrounded by a light-tight box called a dark box. The FGD's front-end electronics resides in 24 minicrates attached to the outside of this box.

Comparing results from the two FGDs provides information on the cross section of neutrino interactions with Carbon and with water, which allows for better understanding of the interactions in Super-Kamiokande.

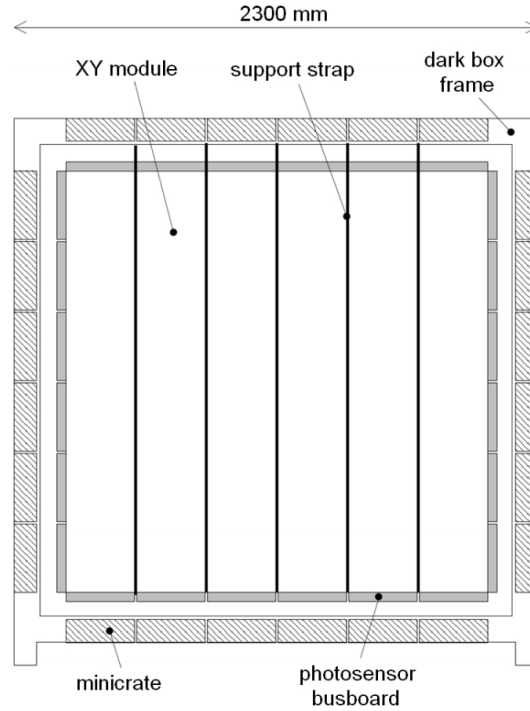


Figure 2.5.: Cross-sectional view of an FGD^[4].

2.2.4. The Electromagnetic Calorimeters (ECal)

The ND280 has two sets of electromagnetic calorimeters, the first set of ECals surrounds the P0D and is used to detect photons and muons escaping the volume of the P0D at high angles, and to veto any particles coming from the outside of the detector. The P0D ECal is made of 6 layers of scintillators separated by 5 layers of 5 mm-thick lead converters.

The second set of ECals is the tracker ECal, it surrounds the TPCs and FGDs and is mainly responsible for tracking particles that emerge from the ND280 tracker (TPCs and FGDs). It is made of 4 cm wide, 1 cm thick plastic scintillator bars arranged in 32 layers and separated by 31 layers of 1.75 mm thick lead sheets^[11]. This design was created to meet the requirement that the tracker ECal detects photons generated in the FGDs and provides muon-pion separation.

2.2.5. The UA1 Magnet

The energy of muons can be measured from the curvature of their tracks in the presence of a magnetic field. Therefore, a 0.2 T dipole magnet (previously used in the NOMAD and UA1 experiments at CERN) is used in the ND280 detector. This magnet also enables the detector to separate particles based on their charge, since different charges bend in opposite curvatures when passing through a magnetic field.

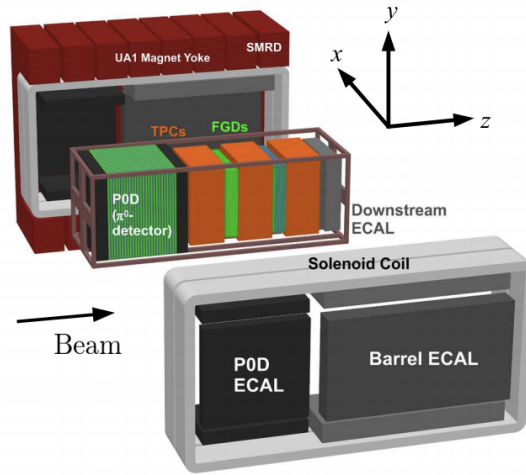


Figure 2.6.: The UA1 magnet^[11].

The UA1 magnet consists of water-cooled Aluminium coils and a flux return yoke. The volume inside the magnet is $7.0 \times 3.5 \times 3.6 \text{ m}^3$. It is made of two halves that enclose the detectors as shown in figure 2.6.

2.2.6. The Side Muon-Range Detector (SMRD)

The SMRD is used in order to detect high angle muons that are missed by the TPCs, as well as to provide a cosmic trigger and veto for the detector. It is created by inserting 0.7 cm thick slabs of a plastic scintillator into the 1.7 cm air gaps between the plates of the magnet.

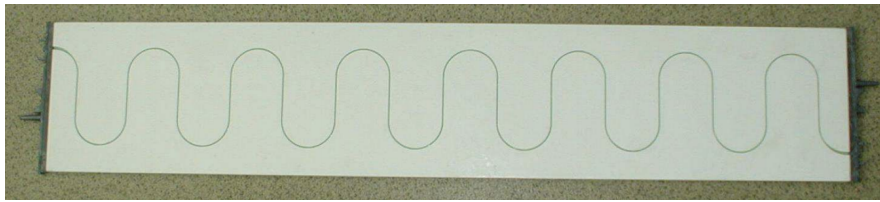


Figure 2.7.: The SMRD scintillator and fiber^[11].

The signal is read out using a WLS fiber that is positioned in an S-shape inside the scintillator in order to cover the largest possible area, see figure 2.7. The two ends of the fiber are connected to MPPCs.

2.3. Neutrino Detection in the ND280

In order to detect neutrinos, they must interact with the material of the detector (water or scintillator). Neutrinos may interact with either the electrons or the nucleons of an atom in charged current or neutral current interactions. In the case of neutrino-nucleon interactions, the most dominant interaction in the energy range of the T2K beam (600 MeV) is the Charged Current Quasi-Elastic (CCQE) interaction, as seen in figure 2.8.

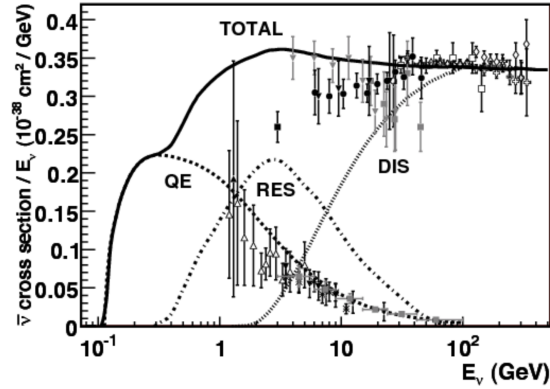


Figure 2.8.: Total neutrino and anti-neutrino per nucleon CC cross sections divided by neutrino energy and plotted as a function of energy, showing the contributions of the quasi-elastic interaction, the resonance interaction, and the deep inelastic scattering^[5].

In the CCQE interaction, a neutrino interacts with a nucleon producing the corresponding lepton. Depending on the type of the neutrino, the interacting neutrons are transformed into protons or vice versa.

$$\nu_l + n \rightarrow l^- + p^+ \quad \text{or} \quad \bar{\nu}_l + p^+ \rightarrow l^+ + n \quad (2.3)$$

When a muon neutrino interacts with one of the FGDs in the ND280 in a CCQE interaction, it produces a muon and a proton. Since both are charged particles, they can be observed in the TPCs as two tracks with opposite curvatures, provided that the angle of the interaction is within the acceptance of the TPCs and the energy is sufficient to emerge from the plastic. The radius of the curvature can then be used to calculate the momenta of the muon and proton. Figure 2.9 shows an example of such event.

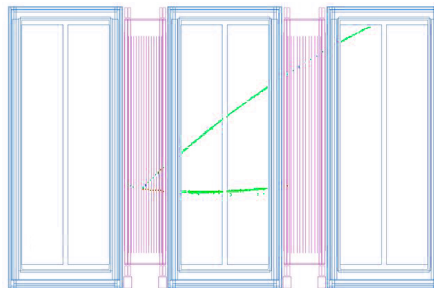


Figure 2.9.: An example of a CCQE neutrino event in the ND280 tracker^[6].

2.4. The ND280 Upgrade

2.4.1. Motivation for Upgrade

With the aim of doing extensive CP violation studies with a 3σ sensitivity, a T2K-II proposal was submitted that requires the increase of the J-PARC beam intensity to run up to 20×10^{21} protons-on-target, which corresponds to an increase of the present exposure by 6 times. A further increase by a factor of 10 is also required by Hyper-Kamiokande*^[3]. These statistics require the reduction of the systematic errors introduced by the configuration of the ND280 from the current value of 6% to around 3%.

One of the approaches considered to reduce these errors is to increase the acceptance for high angle and backward tracks. Although the current ND280 provides excellent efficiency in the forward region, the efficiency suffers significantly for scattering angles larger than 40 degrees, see figure 2.10. This poses the need to use specific models in order to extrapolate the expected spectra observed in the forward-going tracks in the ND280 to the ones seen at Super-Kamiokande, which has a symmetric efficiency with respect to the beam direction^[2].

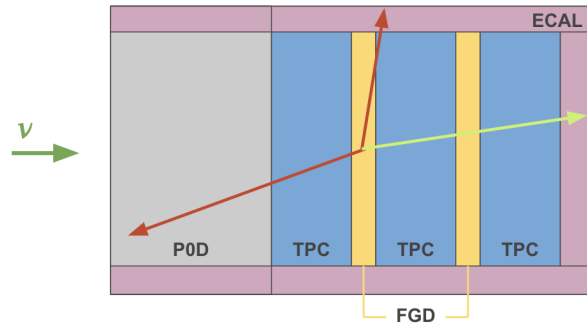


Figure 2.10.: The current ND280 configuration which mainly covers the forward region.

Another limitation in the current design of the ND280 is observed in the FGDs. Since the FGDs act as the target for neutrino interactions, they must be efficient in detecting particles around the interaction vertex. However, their geometry and 2D readout do not provide the best setup for tracking short-ranged particles.

Figure 2.11 shows a sketch of the FGD and a particle track. In the case of the first layer of bars, the signal detected by the highlighted MPPC provides the Z and Y coordinates of the track, while the second layer provides the X and Z coordinates. Therefore, in order to be able to locate the track, it has to cross a minimum of two layers of bars in the FGD. The FGD is further limited when several tracks are produced, in which case the deposited energy cannot be uniquely identified and assigned to a particular spatial direction.

*A planned upgrade to Super-Kamiokande, expected to be an order of magnitude larger.

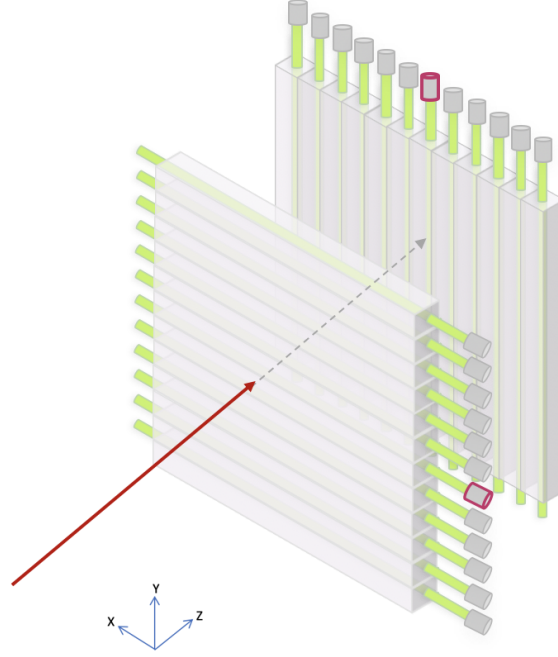


Figure 2.11.: Tracking in the current FGDs. A distance is introduced between the two layers of bars for clarity, this separation does not exist in the real detector.

2.4.2. The Upgraded ND280 Design

To meet these demands, an upgrade project for the ND280 was launched in February 2017. The requirements for the upgraded detector can be summarized in the following points: ^[2]

1. Full acceptance in the polar angle for muons produced in the charged current neutrino interactions.
2. A large mass of a few tons in order to provide a target for neutrino interactions.
3. High efficiency in tracking low energy hadrons around the interaction vertex.
4. Good timing information in order to identify track directions.

The chosen configuration for the ND280 upgrade is shown in figure 2.12. Modifications were introduced to the upstream part, while the current ND280 tracker remains unchanged. Since the P0D has already realized its measurements and is limited by systematics, it is removed from the upgraded ND280 and replaced by three new detectors. A high granularity scintillator detector of a large mass, two high-angle time projection chambers (HA-TPCs), as well as a set of time-of-flight counters.

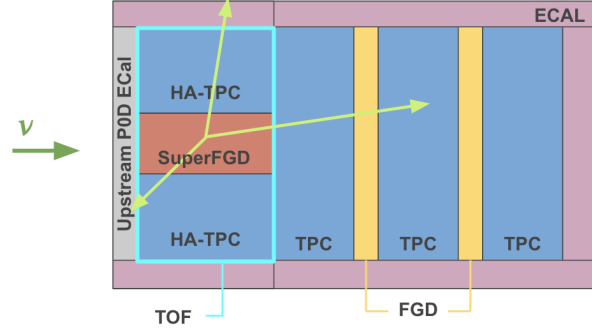


Figure 2.12.: The upgraded ND280 configuration.

The two HA-TPCs are designed based on the existing TPCs with similar features and capabilities. They will be able to provide 3D track reconstruction, as well as charge and momentum measurements for high-angle tracks originating from the new scintillator detector. TPCs are also well suited to track low momentum tracks as those produced in neutrino interactions^[2].

Sandwiched between the two HA-TPCs is the new scintillator detector which acts both as the target for neutrino interactions as well as the detector to reconstruct the tracks around the interaction vertex. To meet these objectives, the scintillator detector is required to have a sufficiently large mass of about 2 tons for its size of $192 \times 192 \times 56$.

Several designs were proposed based on the current technology of using plastic scintillators read out by wavelength-shifting fibers, the selected design for the upgraded ND280 is the SuperFine-Grained Detector (SuperFGD). The SuperFGD is a fully-active detector made of optically-independent cubes. Since this is the subject of this work, it will be described in detail in chapter 4.

Compared to the current FGDs, the SuperFGD has the advantage of providing 3D readout for each 1 cm^3 of the detector volume. Figure 2.13 shows a sketch of one layer of cubes in the SuperFGD. If an interaction occurs in one of the cubes, the energy deposition is read out by 3 orthogonal fibers providing the three coordinates of that cube.

Finally, the Time-of-Flight (TOF) counters are used to determine the direction of the tracks by measuring the crossing time of charged particles compared with the timing information provided by the SuperFGD. This measurement will make it possible to separate neutrino interactions occurring within the detector from any external background, it will also potentially improve particle identification.

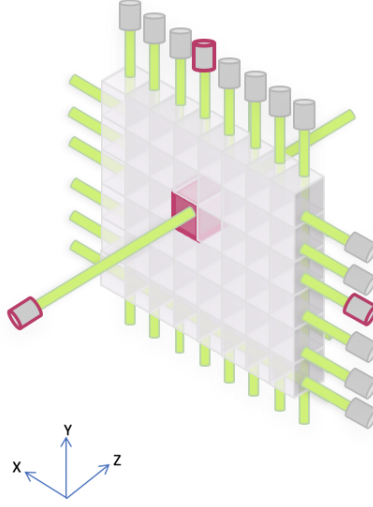


Figure 2.13.: Tracking in the SuperFGD. The rest of the fibers along the Z direction are not drawn for clarity.

In order to evaluate the performance of the new ND280 compared to the current design, a selection of ν_μ Charged-Current interactions has been developed using simulations. For each interaction, the most energetic negative track is selected as the muon candidate. The event is then retained if the muon candidate crosses one of the TPCs active volumes for more than 20 cm and if it is identified as a muon according to the PID algorithms. High angle tracks are also added if the muon candidate enters the ECal and is identified as a muon there^[3].

Figure 2.14 shows the distribution of the muon true momentum versus the polar angle for the selected events for the current and upgraded ND280 designs. According to these figures, the new design clearly shows an improved acceptance for high angle and backward tracks thanks to the addition of the HA-TPCs and the TOF counters.

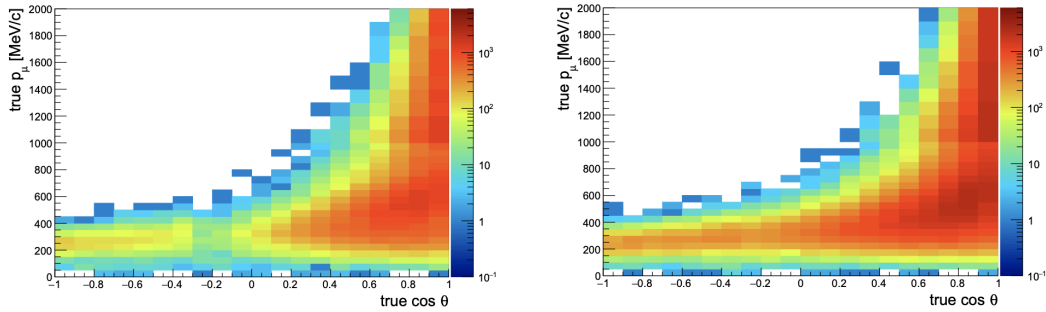


Figure 2.14.: Distribution of selected ν_μ CC events in the two configurations as a function of true muon momentum and polar angle^[3].

And God said:

$$\begin{aligned}\nabla \cdot B &= 0 \\ \nabla \cdot E &= \frac{\rho}{\epsilon_0} \\ \nabla \times E &= -\frac{\delta B}{\delta t} \\ \nabla \times B &= \mu_0 J + \frac{1}{c^2} \frac{\delta E}{\delta t}\end{aligned}$$

And then there was light.

— Anonymous

3

Scintillator Detectors

Contents

3.1. Concept	14
3.2. Proton Interactions in Matter	16
3.3. Birk's Law	17

3.1. Concept

A scintillator is a material that becomes luminescent when it is excited by ionizing radiation. It absorbs the energy deposited by the incoming particle and re-emits it as light. Light emission can occur according to one of two phenomena, fluorescence or phosphorescence. In the case of fluorescence, light is emitted very shortly after the excitation of the scintillating material, whereas for phosphorescence it is delayed by milli-seconds and up to hours.

A good scintillator exhibits a fast response time and a high light yield (i.e. efficient in converting energy to light). These properties, along with their simplicity and low cost, make scintillators a favourable choice for particle detectors. When coupled to a photodetector, photons emitted inside the scintillator can be recorded and converted to an electric signal used to quantify the deposited energy and help identify the particle.

There are two main types of scintillating materials; organic and inorganic. When an incoming particle deposits energy in an organic scintillator, valence electrons transition from molecular orbitals to an excited state. This transition is shortly followed by a decay back to the ground state by emitting photons^[16].

On the other hand, inorganic scintillators have a different scintillation process. These materials feature a band structure. With sufficient energy, an electron in the valence band is excited to the conduction band after crossing a certain energy gap, leaving a hole behind in the valence band. This process is followed by recombination, where an electron in the conduction band loses energy by emitting a photon and falls back to the valence band to re-occupy the energy state of an electron hole^[16]. This causes the response time of inorganic scintillators to be longer, on average, than that of organic scintillators, although it can be tweaked by doping the materials to induce a metastable level between the valence and conduction bands.

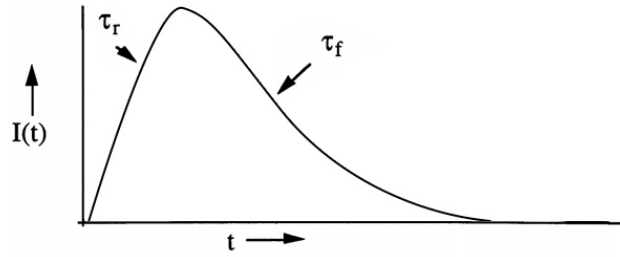


Figure 3.1.: Time profile of the light pulse from a scintillator.

The time profile of the light pulse produced by a scintillator is characterized by a fast rising edge followed by an exponential decay, as shown in figure 3.1. The rising edge depends on the time it takes to populate the excited levels that produce the light emission, which is approximately half a nano-second, whereas the decay time from these levels can be around three or four times longer. Assuming that the rising edge is also exponential, the overall shape of the light pulse can be described by the relation:^[15]

$$I(t) = I_0(e^{-t/\tau_f} - e^{-t/\tau_r}) \quad (3.1)$$

In this experiment, as well as in many particle and nuclear physics applications, plastic scintillators are used. Plastic scintillators are organic scintillators that are known to have a very short response time, fairly high light yield and be cheap and easily shaped into any required form. The density of plastic scintillators ranges between 1.03 and 1.20 g/cm³ with a typical photon yield of 1 photon per 100 eV of deposited energy^[10]. This relatively large density makes them excellent neutrino detectors.

3.2. Proton Interactions in Matter

As a proton traverses through matter, it can lose energy by three types of interactions: interactions with electrons, interactions with the nucleus, and interactions with the atom as a whole. The type of interaction a proton may experience is largely dependant on the energy of the proton. Low energy protons may interact with the atom as a whole, whereas protons of larger energy tend to interact with the electrons and the nucleus. With sufficiently large energies, protons can also interact with the constituents of the nucleus via inelastic scatterings.

The main process by which protons lose energy in a material is through electromagnetic interactions with the electrons. Since the mass of a proton is much larger than the mass of an electron, protons only lose a small fraction of their energy in these soft EM collisions. Scatterings, in this case, are also of very small angles^[9].

Depending on the proton's energy, nuclear interactions may be elastic and cause scatterings with large angles compared to scatterings with electrons, or they may be inelastic and produce secondary particles like pions. Since nuclear interactions do not follow any simple theory, identifying and separating them from other sources of energy losses is very important in order to extract interaction cross sections.

When protons pass through a material, they slow down by ionizing its atoms. In a scintillator, this ionization produces light quanta in the visible range. As the proton loses energy and slows down, its stopping power* increases causing higher ionization density due to the increased interaction cross sections. Consequently, protons deposit the most energy right before they stop. Figure 3.2 shows the relation between the stopping power and the energy of the proton in polystyrene (the plastic material used for the SuperFGD cubes).

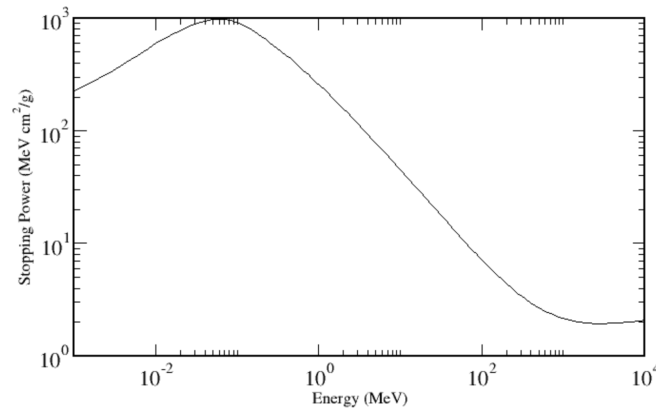


Figure 3.2.: The stopping power (in polystyrene) as a function of the proton's energy^[28].

*The retarding force acting on charged particles due to their interaction with matter, resulting in a loss in the particle's energy.

3.3. Birk's Law

The response of plastic scintillators to the ionization density (dE/dx) is not linear. The relationship between the light yield in a scintillator and the amount of energy loss a particle undergoes as it traverses through it is described by Birk's law:

$$\frac{dL}{dx} = S \frac{\frac{dE}{dx}}{1 + K_B \frac{dE}{dx}} \quad (3.2)$$

Where L is the light yield, S is the scintillation efficiency, dE/dx is the energy loss of the particle per unit length and K_B is Birk's constant which depends on the material.

In the limit of low values of dE/dx , equation 3.2 reduces to $dL/dx = S dE/dx$ and the relation between the light yield and energy loss is linear. On the other hand, for large values of dE/dx the equation reduces to a constant value of $dL/dx = S/K_B$. Consequently, the linearity is lost and saturation is reached^[7]. Figure 3.3 shows the relation between the scintillation energy and the energy loss per unit length as per Birk's theory.

According to Birk, the non-linearity in the response of the scintillator, when the density of the energy loss is high, is due to recombination and quenching effects between the excited molecules which reduce the light yield. In such zones, the excitation of the molecules in the scintillator reaches saturation. Once saturation is reached, any further energy deposition would be dissipated non-radiatively (as lattice vibrations or heat).

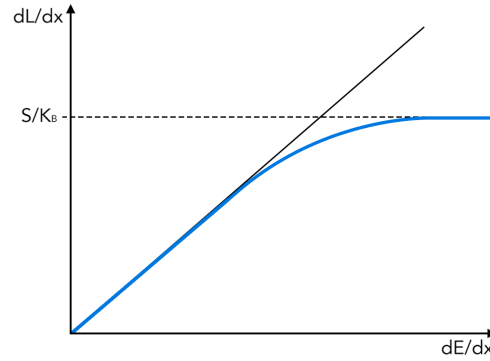


Figure 3.3.: The relation between the scintillation energy and the energy loss per unit length as per Birk's theory.

In an infinite material and for the same deposited energy, particles with higher dE/dx (eg. protons) would produce lower light yield per unit of energy than particles with lower dE/dx (eg. electrons). Note that K_B does not depend on the particle type.

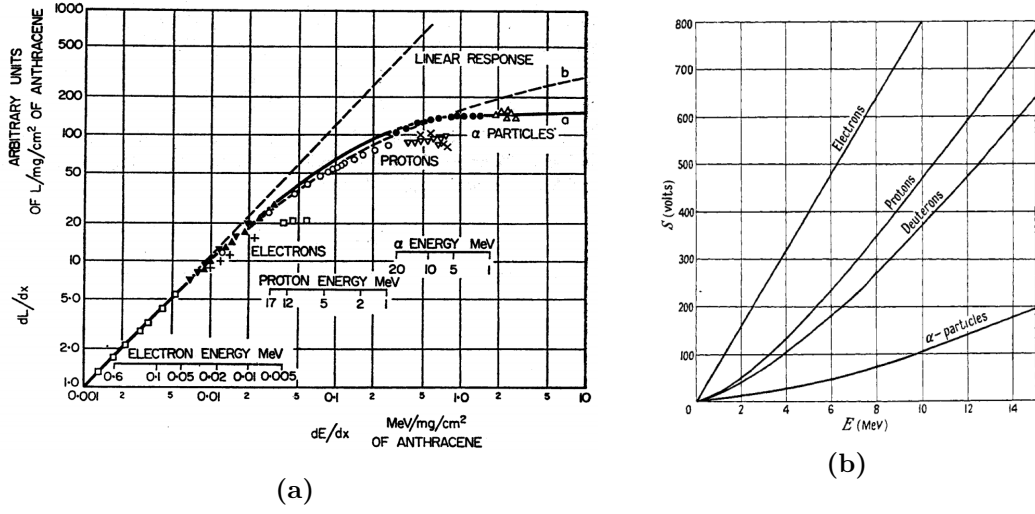


Figure 3.4.: (a) dL/dx as a function of dE/dx for different particles in Anthracene^[8]. (b) Relative scintillation response S of Anthracene to different particles of energy E ^[7].

This can be worked out from the Birk's formula as follows:

$$\frac{(dL/dE)_p}{(dL/dE)_e} = \frac{1 + K_B(dE/dx)_e}{1 + K_B(dE/dx)_p} < 1 \quad (3.3)$$

Birk was able to prove these results by studying scintillation in Anthracene; a scintillating organic crystal. Figure 3.4 (a) shows the nonlinearity of the light yield using different types of particles. Figure 3.4 (b) shows the relative scintillation response S as a function of the energy for different particles. It can be clearly observed that electrons have a linear response whereas particles with higher dE/dx do not respond linearly.

*For me, it is far better to grasp the Universe as
it really is than to persist in delusion, however
satisfying and reassuring.*

— Carl Sagan

4

The SuperFGD

Contents

4.1. The Scintillating Cubes	20
4.2. Wavelength-Shifting Fibers	20
4.3. Multi-Pixel Photon Counters	23
4.4. The Mechanical Box	27
4.5. The Readout Electronics	28
4.6. The SuperFGD Prototype	31
4.6.1. Assembly	31
4.6.2. Prototype Electronics	32
4.6.3. Data Acquisition (DAQ) and Recorded Data	33
4.6.4. Data Structure	36
4.6.5. Calibration	36

The SuperFine-Grained Detector is the active target for neutrino interactions in the upgraded ND280 detector^[3]. It is a plastic scintillator detector composed of a large number of optically independent $1 \times 1 \times 1 \text{ cm}^3$ cubes read out along three orthogonal directions by wavelength-shifting fibers, see figure 4.1. The SuperFGD is a fully-active detector with isotropic acceptance, its fine granularity, along with its 3D readout, allows for reconstructing short tracks around the interaction vertex.

Each fiber has a multi-pixel photon counter (MPPC) attached to one of its ends. The MPPCs will be placed on the upstream, top, left and right sides of the detector and the front-end electronics will be divided between the left and right sides. The analog signal from the upstream and the top face will be routed to the left or right side for readout^[3].

4.1. The Scintillating Cubes

The building blocks of the SuperFGD are the scintillating cubes. The 1 cm cubes are made of polystyrene and doped with 1.5% of paraterphenyl (PTP) and 0.01% of POPOP^[3]. To reduce the amount of light leaking from the cubes, they are coated with a 50-80 μm thick chemical reflector by etching their surface with a chemical agent that creates a white micropore deposit over the polystyrene.

The cubes are produced by Uniplast in Vladimir, Russia. For the first prototypes, the cubes were made by cutting 1 cm thick slabs into $1 \times 1 \times 1 \text{ cm}^3$ cubes*. Following the production phase, each cube is drilled to create three orthogonal cylindrical holes of 1.5 mm diameter along each of the three axes with a distance of 3 mm between the hole axis and the closest edge of the cube. These holes are used for the insertion of the wavelength-shifting fibers. Figure 4.1 shows a sketch for the cube with the 3 orthogonal fibers inserted into the holes, as well as an array of cubes after assembly.

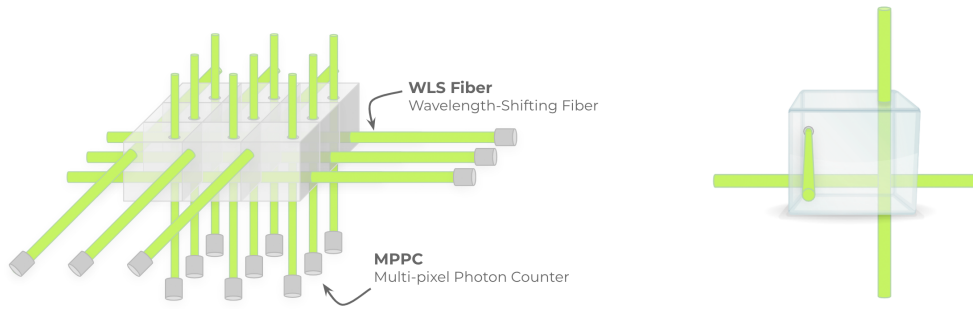


Figure 4.1.: SuperFGD cube and cube array with WLS fibers inserted.

For a detector of size $192 \times 192 \times 56 \text{ cm}^3$, the number of cubes needed is 2,064,384.

4.2. Wavelength-Shifting Fibers

The use of wavelength-shifting fibers is an efficient solution for collecting the light emitted in a row of cubes and transporting it to the readout at one side of the fiber. The fibers used in the SuperFGD are the Y-11(200) Multi-cladding S-type 1 mm diameter fibers produced by Kuraray.

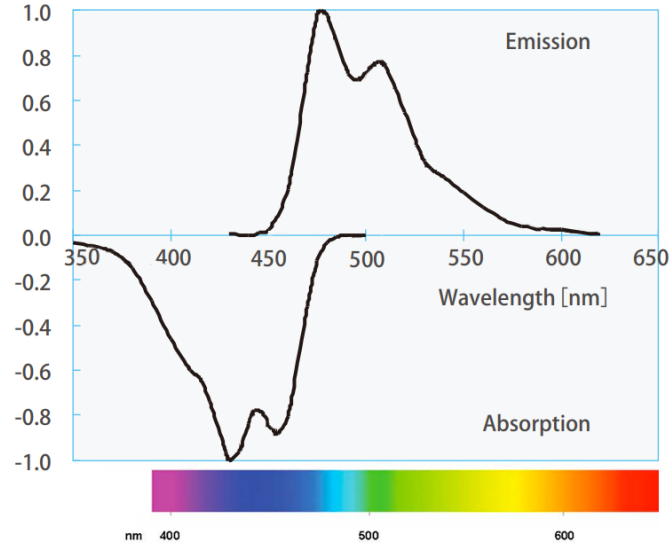
The Y-11(200)M are green wavelength-shifting fibers with a 200 ppm concentration of the K27 dye, they have a peak absorption wavelength of 430 nm and a peak emission wavelength of 476 nm. Other specifications for these fibers are detailed in table 4.1^[17].

*For the actual detector, a different technique using injection molding has been adopted. This method decreases the production costs and the micro variations between cube sizes.

Table 4.1.: Properties of the Y-11(200)M WLS fibers.

Item	Specification
Fiber type	Round shape, Multi-cladding
Diameter	1.0 mm
Materials	Core: Polystyrene (PS), Middle clad: Polymethylmethacrylate (PMMA), Outer clad: Fluorinated polymer (FP)
Refractive index	Core: 1.59, Middle clad: 1.49, Outer clad: 1.42
Trapping efficiency	5.4%
Attenuation length	>3.5 m

When the violet/blue light emitted inside a cube enters one of the fibers, it is absorbed by the dye molecules and then re-emitted uniformly with a longer wavelength (i.e it is shifted towards green). The new emission is now trapped within the fiber due to total internal reflections, as it travels to the ends of the fiber. Figure 4.2 shows the absorption and emission spectra of the Y-11(200)M WLS fibers.

**Figure 4.2.:** Y-11(200)M fibers absorption and emission spectra^[17].

As the light travels across the fiber, it is attenuated causing a reduction in its intensity. Attenuation in fibers is shown to be caused primarily by both scattering and absorption. Figure 4.3 shows the effect of the attenuation on the intensity of the light, the data in this figure was produced by applying UV light to one end of the fiber and reading it using an optical spectrum analyzer on the other end. The four tested fibers were all of 1 mm diameter, and their lengths were 10, 30, 100 and 300 cm.

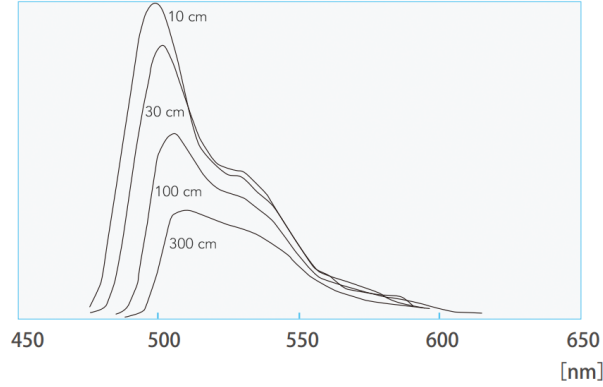


Figure 4.3.: Emission spectra for the Y-11(200)M fibers for different fiber lengths^[17].

The attenuation in the SuperFGD fibers was studied further by INR-Russia^[18]. Their results show that the attenuation in the Y-11(200)M fibers is best described by the function:

$$LY(x) = LY_S e^{-x/L_S} + LY_L e^{-x/L_L} \quad (4.1)$$

Where light is attenuated in different fractions (LY_S and LY_L) and by different attenuation lengths (L_S and L_L) for short and long wavelengths. The tests were performed on 2 m long fibers using a UV LED. Figure 4.4 shows the light yield recorded when the UV light was positioned at different distances from the MPPC placed at the end of the fiber. Two configurations were tested, one with a reflector on the other end of the fiber (red) and one without a reflector (blue). A reflector at the fiber end gives 30-50% more light yield in a 2 m long fiber.

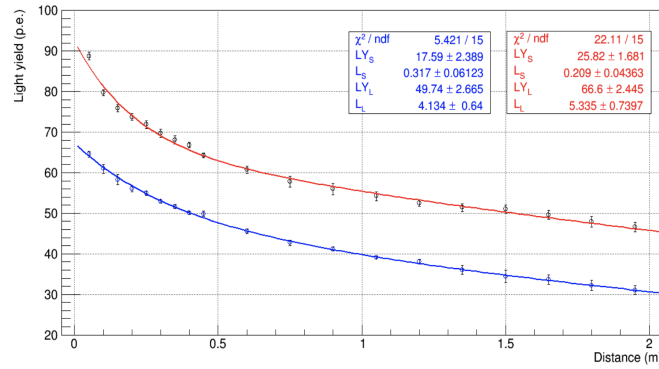


Figure 4.4.: Attenuation in a 2 m long fiber^[18].

The total length of fiber required for the SuperFGD will be 70 km, including spares. The longest fibers will be around 2 m in length.

4.3. Multi-Pixel Photon Counters

In order to convert the light from the WLS fibers into an electric signal, each fiber is read out on one end by a Multi-Pixel Photon Counter (MPPC). MPPCs (also known as silicon photomultipliers or SiPMs) are solid-state photodetectors that consist of an array of avalanche photodiodes (APDs) sitting on a common substrate and operating in the Geiger mode. When an MPPC absorbs a photon, it produces a current pulse that lasts several tens of nanoseconds with a gain between 10^5 and 10^6 , depending on the bias voltage and environmental conditions.

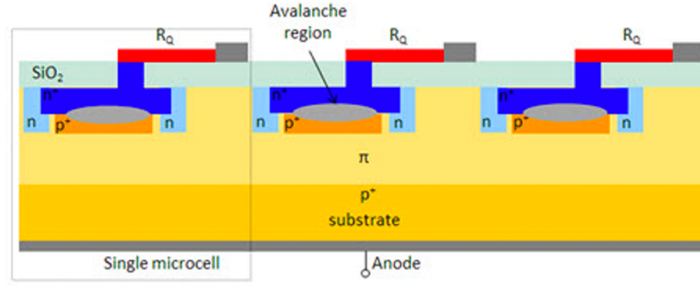


Figure 4.5.: The structure of an MPPC^[19].

Figure 4.5 shows the cross-section of an MPPC containing 3 microcells. Each microcell consists of one APD and a quenching resistor R_Q , whose function is described below. The APD has a p-n junction under a reverse bias voltage that is above its breakdown voltage, making it act as a diode. Operating the APD with this condition ensures high gain for a single photon.

When a photon enters the Silicon layer on the APD, it creates an electron-hole pair via the photoelectric effect. These electrons are then affected by the high electric field in the depletion region of the p-n junction and are accelerated causing them to collide and create new electron-hole pairs (impact ionization). This process would trigger an avalanche in the junction which produces a high exponential gain that can reach 10^5 to 10^6 electrons for one photon.

Once the APD is in avalanche mode, if the charge carriers are extracted at a rate lower than the rate of impact ionization, the avalanche would be sustained. However, this would introduce two disadvantages:

1. The current created by the avalanche rises swiftly to a steady value that would remain constant regardless of the number of photons that arrive to the pixel. Therefore, during the avalanche, the APD would be insensitive to new signals. If a new photon falls on the same pixel of the MPPC, it would not trigger a new signal.
2. If the pixel remains in avalanche for a long period of time, this would heat the device and may cause thermal damage.

In order to overcome this, a quenching resistor R_Q with high resistance is used to introduce a voltage drop that would bring the APD back to the bias voltage making it ready to accept new signals. In summary, an MPPC acts as a photon counter such that each photon is detected by a single pixel.

The high gain of the APDs, coupled with fast extraction rates, makes MPPCs excellent for single photon detection. These devices are also characterized by high detection efficiency, excellent timing resolution, low operation voltages, and immunity to magnetic fields. Furthermore, MPPCs offer much easier mechanical integration compared to the traditional Photomultiplier tubes (PMTs).

There are a few properties of MPPCs that determine their performance in photon detection, these properties can be summarized as follows:

1. Gain

When a certain pixel in the MPPC receives a photon, it produces a Geiger-discharge in a similar way to the discharge of a capacitor with capacitance C_j .

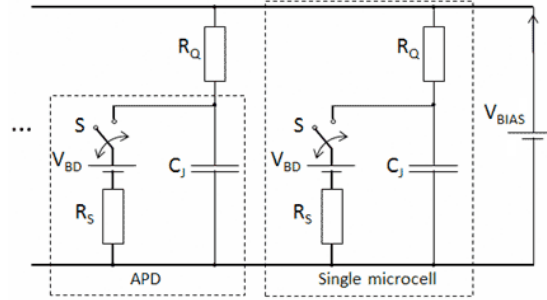


Figure 4.6.: The equivalent circuit for a subset of MPPC cells^[19].

Figure 4.6 shows the equivalent circuit for an MPPC where R_S is the resistance of the APD, V_{BD} is the breakdown voltage, C_j is the capacitance of the junction and S is a switch that closes when a photon is received. The gain of one pixel can be obtained by calculating the charge of the capacitor C_j as follows:

$$G = \frac{Q_{out}}{e} = \frac{I_{max} \cdot \tau}{e} = \frac{V_{BIAS} - V_{BD}}{R_Q + R_S} \frac{R_Q C_j}{e} \approx \frac{\Delta V \cdot C_j}{e} \quad (4.2)$$

Since $R_Q \gg R_S$.

The term $\Delta V = V_{BIAS} - V_{BD}$ is known as the *overvoltage*. Since C_j is set by the specifications of the MPPC, equation 4.2 shows that the gain varies linearly with the overvoltage. If more than one pixel received photons at the same time, the charge output of the MPPC will be a multiple of Q_{out} . Which means that an MPPC is basically a photon counter.

2. Photon Detection Efficiency (PDE)

PDE is the probability that an MPPC produces an output signal in response to an incident photon. In order for a photon to produce a signal, it must create an electron-hole pair which must, in turn, trigger an avalanche. Since a higher electric field in the junction increases the probability of an avalanche, the photon detection efficiency increase with increasing overvoltage (ΔV) as shown in figure 4.7.

Another factor that contributes to the PDE is the geometrical efficiency introduced by the fill factor. The fill factor of an MPPC is the ratio of the active area of a pixel to its total area, a high fill factor corresponds to a larger sensitive area and therefore a higher detection efficiency.

3. Optical Crosstalk

Optical crosstalk occurs when an avalanche in one pixel triggers secondary avalanches in one or more adjacent pixels. The secondary avalanches may be nearly simultaneous with the primary (direct or prompt crosstalk) or delayed by several tens of nanoseconds (delayed crosstalk).

The probability for crosstalk depends on three factors; the layered structure of the MPPC, the size of a pixel, and the overvoltage. Since the first two parameters are fixed for a certain MPPC, the probability for optical crosstalk is mainly controlled by the overvoltage and it increases with increasing ΔV as shown in figure 4.7.

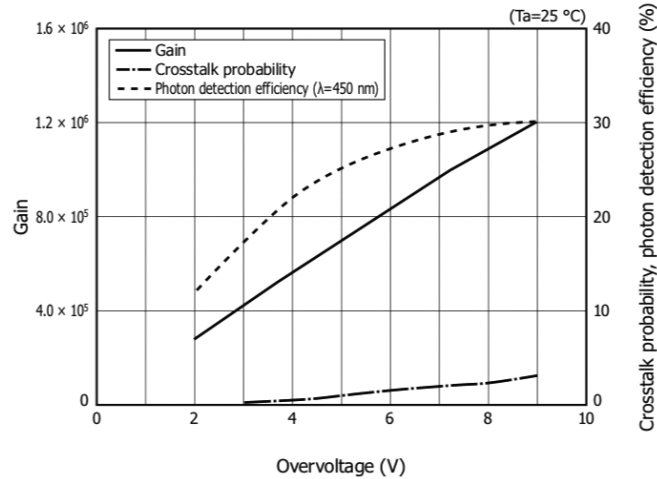


Figure 4.7.: Overvoltage specifications of gain, crosstalk and PDE^[20].

4. Dark Counts

Even in the absence of light, some charge carriers may be created in the junction due to thermal effects which would generate current pulses known as dark counts. The rate of dark counts increases with both temperature and the overvoltage, since ΔV introduces an electric field that assists in producing an avalanche.

The occurrence of dark counts follows a Poisson distribution, this distribution represents the internal noise of the detector.

5. After-pulsing

While a certain pixel is in avalanche, some charge carriers may be captured in the depletion region by traps caused by impurities in the silicon. These carriers are later released, re-triggering the avalanche and generating an afterpulse. The probability for an afterpulse depends on various parameters such as the density of impurities in the silicon, the gain, the energy level of the trap in the band gap and the strength of the electric field in the depletion region (and therefore, ΔV).

6. Dynamic Range

The dynamic range of an MPPC is the optical signal range over which the sensor provides a useful output. It depends on the total number of pixels in the MPPC, the overvoltage and the wavelength of the incident photon. More pixels result in a higher dynamic range.

The relation between the number of incident photons (N_{photon}) and the number of fired pixels (N_{fired}) can be described by^[22]:

$$N_{fired}(N_{total}, \Delta V, \lambda) = N_{total} \left[1 - e^{\frac{-N_{photon} \times PDE(\Delta V, \lambda)}{N_{total}}} \right] \quad (4.3)$$

where N_{total} is the total number of pixels in the MPPC.

7. Recovery Time

The development of the avalanche in a depletion region of very small width is very fast. The rising time of the signal is very short (~ 1 ns) and the falling time is determined by the constant $C_j \cdot R_S$ and is of the order of tens of nanoseconds. This means that a single pixel in an MPPC can record a signal and recover within a time < 100 ns. Since a higher electric field in the depletion region makes the impact ionization faster, a higher overvoltage is expected to decrease the recovery time.

8. Time Resolution (of a single cell)

The avalanche development may have some time fluctuations that cause time jitter in the output signal of a single pixel. One factor that may cause such time jitter is the creation of the electron-hole pair far from the depletion region where the avalanche is to be triggered. In this case, the charge carriers must drift to the depletion region introducing a time difference between the arrival of the photon and the beginning of the avalanche.

Figure 4.8 (a) shows the current-voltage dependence of an MPPC pixel. Upon receiving a photon, the avalanche causes a discharge that is quenched by the resistor R_Q back to the bias voltage V_{BIAS} .

Figure 4.8 (b) shows the typical pulse shape for a single photon in an MPPC, which is characterized by a steep leading edge followed by a long exponential falling edge. The recharge time is determined by the RC constant of the circuit, during which no new photons are detected.

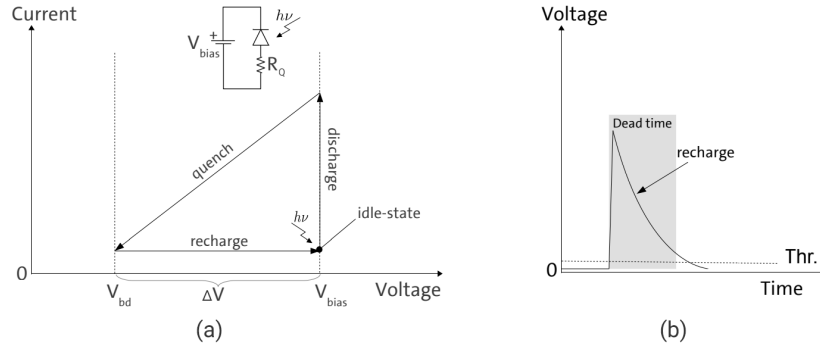


Figure 4.8.: (a) I-V dependence of an MPPC pixel, (b) Pulse shape for a single photon ^[21].

The MPPCs used in the SuperFGD are the S13360-1325PE surface mounted MPPCs by Hamamatsu. The specifications of these MPPCs at 25° C are detailed in table 4.2. The SuperFGD would require a total of 58,368 MPPCs.

Table 4.2.: Properties of the S13360-1325PE MPPCs ^[20].

Item	Specification
Effective photosensitive area	1.3 mm × 1.3 mm
Pixel Pitch	25 μm
Number of Pixels	2668 pixels
Spectral Response Range	320 - 900 nm
Peak Sensitivity Wavelength	450 nm
Photon Detection Efficiency	25%
Gain	7.0×10^5
Crosstalk Probability	1%
Breakdown Voltage	53 ± 5 V
Recommended Operation Voltage	$V_{BD} + 5V$
Typical Dark Count Rate	70 kcps

4.4. The Mechanical Box

In order to support the 2-ton SuperFGD while minimizing the dead space in the ND280 detector, a mechanical box is being developed to host the scintillating cubes along with the optical interface.

The panels are made of a 16 mm thick AIREX core sandwiched between two 2 mm thick carbon fiber layers, all glued together, with an array of 3 mm diameter holes spaced 1 cm apart in order to extend the WLS fibers to the optical interface on the external side of the panel.

This optical interface will be attached to four sides of the box. Each fiber will be glued to an optical connector that ensures the alignment of the fiber and the MPPC. The MPPCs will be soldered to Printed Circuit Boards (PCBs) as shown in figure 4.9. The dimensions of the box, including the optical interface, are $2018 \times 640 \times 2018$ mm³ [3].

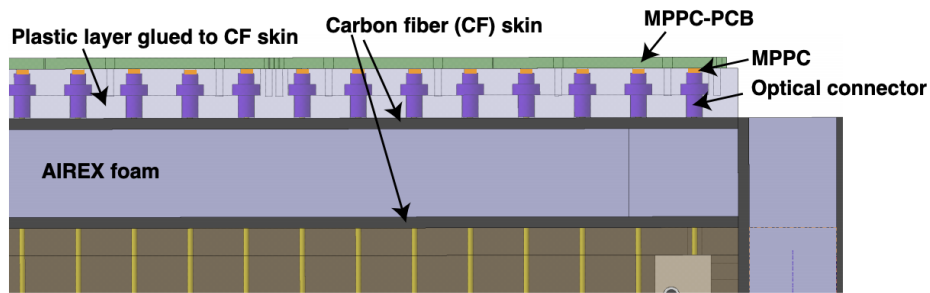


Figure 4.9.: The cross-section of the box and optical interface [3].

4.5. The Readout Electronics

The readout electronics system of the SuperFGD is based on the CITIROC (Cherenkov Imaging Telescope Integrated Readout Chip) used by the Baby MIND collaboration (WAGASCI J-PARC experiment E69). Each CITIROC chip contains 32 channels that correspond to 32 MPPCs. The block diagram of a CITIROC is shown in figure 4.10.

A common high voltage is applied externally to all MPPCs. To modify the operating voltage for individual MPPCs, the CITIROC chip is equipped with a 4.5 V range 8-bit Digital-to-Analogue converter (DAC) per channel. These input DACs have 9 control bits; 1 to enable/disable the DAC and 8 to set the voltage.

Each MPPC signal goes through two voltage-sensitive pre-amplifiers with different gain (high gain and low gain) that ensure the detection of charges from 160 fC to 320 pC. The high gain (HG) signal is connected to a 15 ns fast shaper and two discriminators. The first one is used to form a trigger line that records a rising edge if the amplitude of the signal exceeds the threshold of the discriminator. While the second is used to record the timing information of the signal (rising edge and falling edge). Each of these discriminators is connected to a 4-bit DAC that can be used to change the discriminator threshold for individual channels. At the end, each of them gives a digital output, this output is multiplexed in the case of the trigger line.

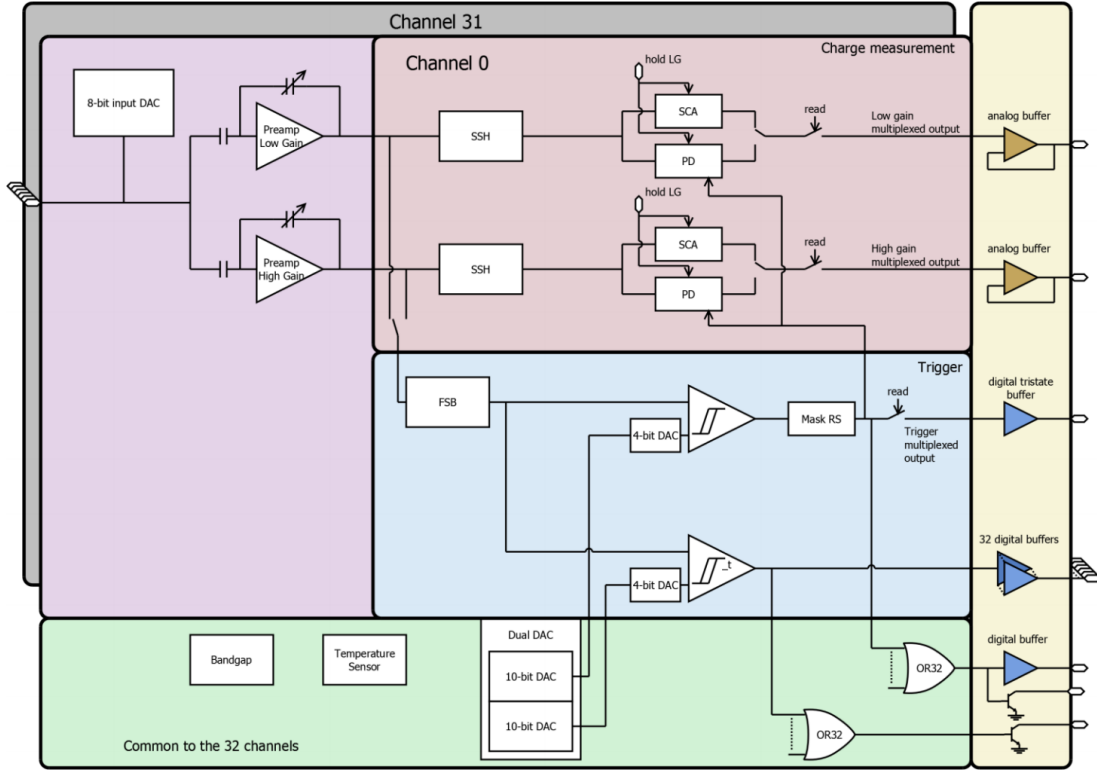


Figure 4.10.: The block diagram of a CITIROC^[23].

Both the high gain and low gain pre-amplifiers are also connected to two variable slow shapers and two Track and Hold blocks. When a rising edge is recorded on the trigger line, all 32 channels start sampling the amplitude for a certain duration set by the Hold. The two signal paths give two independent multiplexed analogue outputs for the HG and LG.

A number of CITIROC chips (4 to 8) are connected to one Front-End Board (FEB) along with a 12-bit, 8-channel Analogue-to-Digital converter (ADC) to digitize the analogue HG and LG signals from the CITIROC, an FPGA Altera Aria X to control and manage the timing and data flow from the CITIROCs and the ADC, and an optical link to transmit the data to a data acquisition system^[3]. A sketch for the FEB is shown in figure 4.11.

Each group of 32 channels is connected to one CITIROC via a 2 m long coaxial cable bundle. Amplifying the signal at the FEB end instead of the MPPC end has the advantage of allowing the transmission of the signal from the MPPC to the FEB in current-mode with excellent noise immunity.

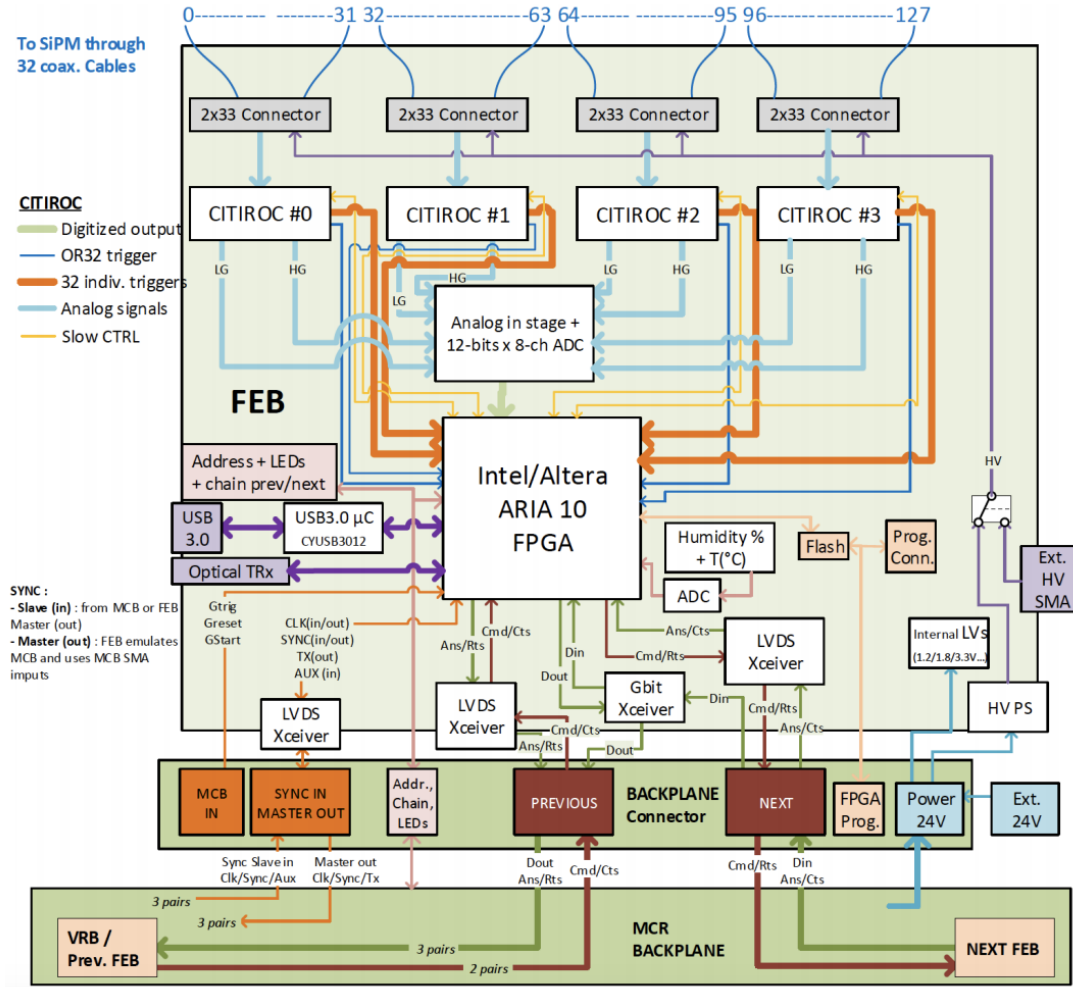


Figure 4.11.: A sketch for the SuperFGD FEBs^[3].

Because of the multiplexing and digitization stages, the analogue signals from the HG and LG lines suffer from a dead time of $9 \mu\text{s}$. On the other hand, the digital signal with the timing information is continuously sampled by the FPGA at a rate of 400 MHz. This proves useful when two hits occur on one fiber within a time period less than the dead time. In this case, the time difference between the rising and falling edge (known as the Time-over-Threshold [ToT]) can be used as an indication of the amplitude of the signal.

Due to space limitations around the ND280 detector basket, the readout electronics are going to be placed in towers to the left and right sides of the SuperFGD. There will be a total of 8 towers on each side, each tower will host 30 FEBs that are connected via a backplane. To synchronize the data acquisition with the T2K beam and other ND280 systems, a Master Clock Board (MCB) along with fanout boards are used.

4.6. The SuperFGD Prototype

Two prototypes for the SuperFGD were built and tested. The first prototype was a small $5 \times 5 \times 5 \text{ cm}^3$ detector made of 125 cubes and tested in autumn 2017. The second prototype is a $24 \times 8 \times 48 \text{ cm}^3$ detector consisting of 9216 cubes and tested at CERN in the summer of 2018. This study is conducted with the data of the latter prototype.

4.6.1. Assembly

The SuperFGD prototype II was built at INR, Russia. The dimensions of this prototype were chosen such that it would fit inside the MNP17 magnet[†] during the test beam at CERN. It was assembled using fishing lines by building two-dimensional arrays of 24×48 cubes using a flexible plastic thread of 1.3 mm diameter inserted through the holes in the cubes. Once 8 of these arrays were built, they were stacked on top of each other with layers of Tyvek paper reflector between each two arrays. The Tyvek layers were used in the prototype in order to test for their efficiency in reducing crosstalk and containing the light in that layer of cubes. The last step in the assembly was to remove the fishing lines and replace them with the Y-11(200)M WLS fibers^[3].

Following the assembly, the prototype was sent to CERN in May 2018 where it was equipped with photosensors and electronics. Three types of MPPCs were used for comparison, the majority were of the same type chosen for the ND280 upgrade (S13360-1325CS, though in a different package, ceramic rather than surface mounted). Table 4.3 shows the specifications of the three types of MPPCs used.

Table 4.3.: Properties of the SuperFGD Prototype II MPPCs^[3].

Hamamatsu ref.	S13360-1325CS	S13081-050CS	S12571-025C
Usage	SuperFGD	WAGASCI SMRD	Baby MIND
Prototype ref.	Type I	Type II	Type III
Numbers in proto.	1152	384	192
Package	Ceramic	Ceramic	Ceramic
Pixel pitch [μm]	25	50	25
Number of pixels	2668	667	1600
Active area [mm ²]	1.3×1.3	1.3×1.3	1.0×1.0
Operating voltage [V]	56 → 58	53 → 55	67 → 68
PDE [%]	25	35	35
Dark count rate [kHz]	70	90	100
Gain	7×10^5	1.5×10^6	5.15×10^5
Crosstalk probability [%]	1	1	10

[†]A general purpose horizontal dipole magnet with a maximum field of 0.96 T, and a gap 30 cm high, 1 m wide and 52 cm long

MPPCs of type II were installed on the upstream top and bottom channels, MPPCs of type III were installed in the middle top and bottom channels, and MPPCs of type I were used for all other channels. The locations of the MPPCs are shown in figure 4.12.

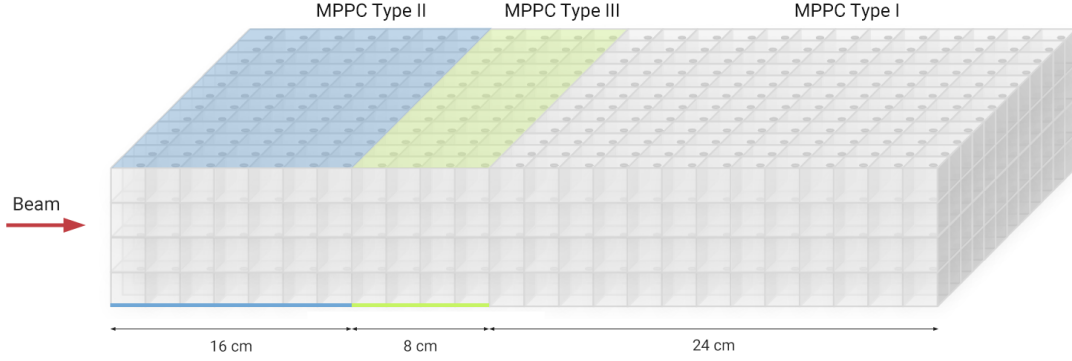


Figure 4.12.: MPPC positions on the SuperFGD prototype (The detector is drawn at 0.5 scale).

4.6.2. Prototype Electronics

The readout electronics of the detector were developed at the University of Geneva for the Baby MIND detector. Three CITIROC ASICs are installed on each FEB along with an 8-channel ADC and an FPGA Altera Aria V. Groups of 4 or 5 FEBs are then installed in 4 minirates and connected via a backplane that hosts a USB3 microcontroller to transmit the data to the DAQ system with speed up to 3.2 Gbit/s. Each FEB reads a total of 96 channels. A photograph of the FEBs used in prototype II is shown in figure 4.13 (b).

The prototype was equipped with 19 FEBs, 18 of which were connected to channels and used for MPPC readout. The remaining FEB (with ID 12) was connected to an external set of detectors used as a triggering system.

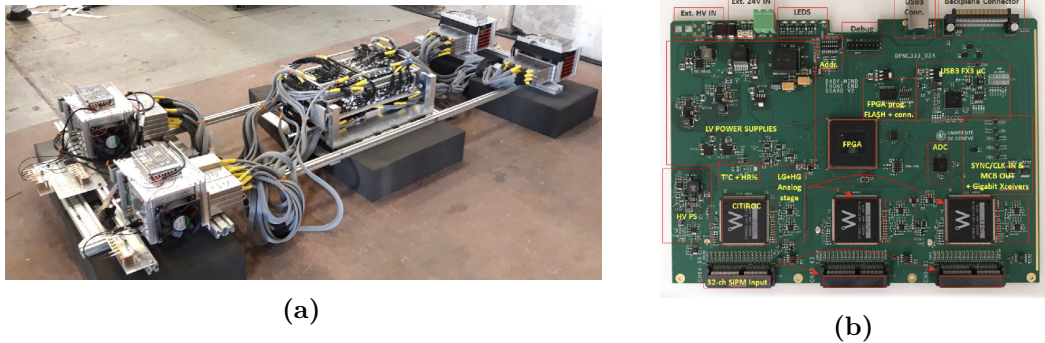


Figure 4.13.: (a) Photo of the SuperFGD Prototype II after full assembly. (b) Photo of the FEBs used in prototype II^[23].

4.6.3. Data Acquisition (DAQ) and Recorded Data

The DAQ software was developed at the University of Geneva for the Baby MIND detector. Each one of the four minicrates (MCRs) is connected to the DAQ PC via USB3 cables. The DAQ can be started by loading a configuration file that contains all the settings for the FEBs, such as the discriminator thresholds and the HG and LG values for the channels of the detector. Once the file is loaded and the connection to all four MCRs is established, the DAQ may be started.

Table 4.4.: SuperFGD hit data.

Hit Data	Description
Serial Number	The ID number of the FEB that has recorded the hit.
Channel	The ID number of the channel that has recorded the hit.
Spill Tag	The number of the spill during which the hit was recorded.
Spill Time	The starting time of the spill in units of [10 ms].
Spill Trail Time	The ending time of the spill in units of [10 ms].
GTrigTag	The tag assigned by the global trigger in units of [10 μ s].
Time From Spill	The hit time from the beginning of the spill in units of [2.5 ns].
Lead Time	The rising edge trigger sampling time in units of [2.5 ns].
Trail Time	The falling edge trigger sampling time in units of [2.5 ns].
ToT	The Time-over-Threshold in units of [2.5 ns].
HG Amplitude	The high gain analogue amplitude in units of [ADC].
LG Amplitude	The low gain analogue amplitude in units of [ADC].

Simultaneously, a command is issued by the Master Clock Board (MCB) in order to synchronize all FEBs. The MCB is synchronized with the beam through a pulse generator that generates a pulse of a certain width upon receiving a trigger for the beam arrival. The width of that pulse corresponds to the data acquisition window for each spill. The MCB is then connected to the four MCRs through a fanout board and RJ45 cables[‡]. Once the data acquisition is started, a check is performed to ensure that all MCRs are properly synchronized. Four separate data files are then written to the PC; one for each MCR. Table 4.4 shows the information recorded by the DAQ software for each hit.

Figure 4.14 shows a detailed description of how the timing information of a hit is recorded. And figure 4.15 shows the description of the recording of the hit amplitude.

[‡]Ethernet cables with Registered Jack-45 (RJ45) connectors.

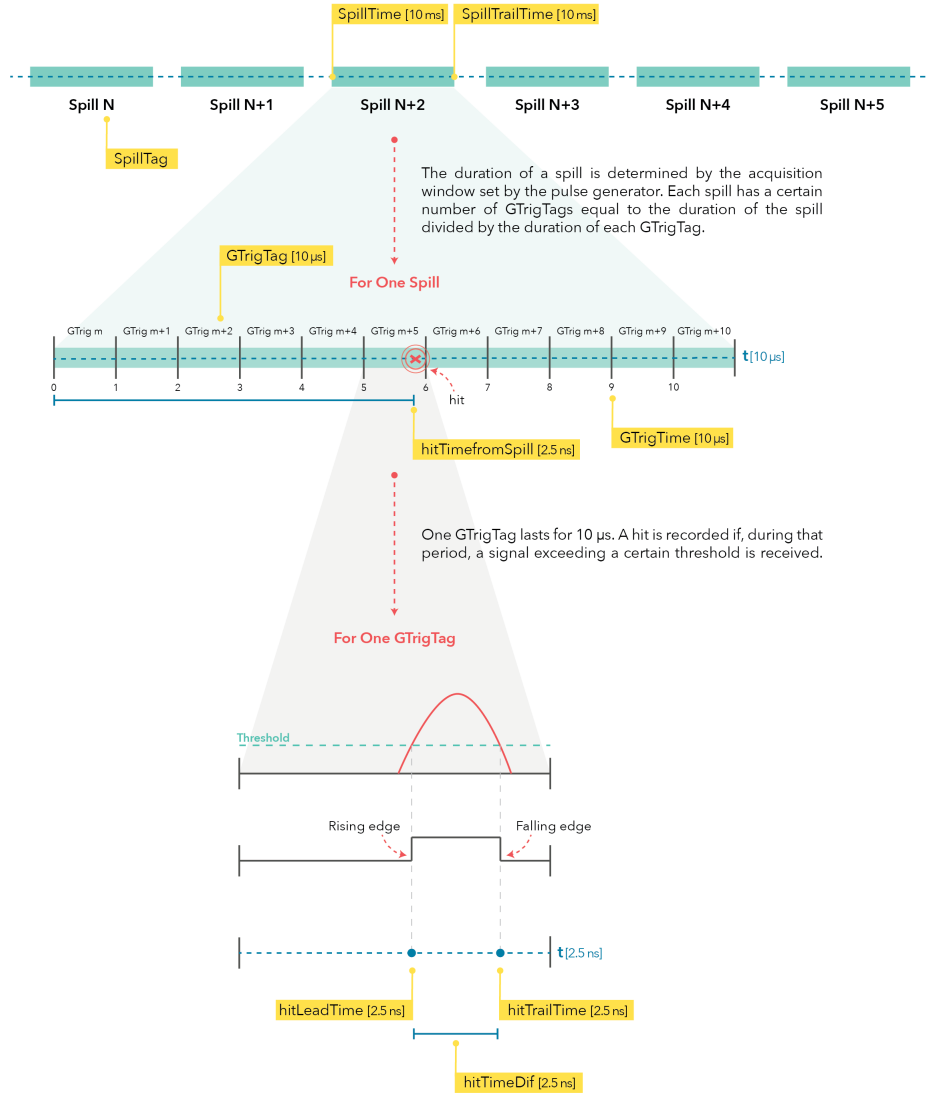


Figure 4.14.: The recorded timing information of a hit, the numbers in brackets refer to the resolution of each value.

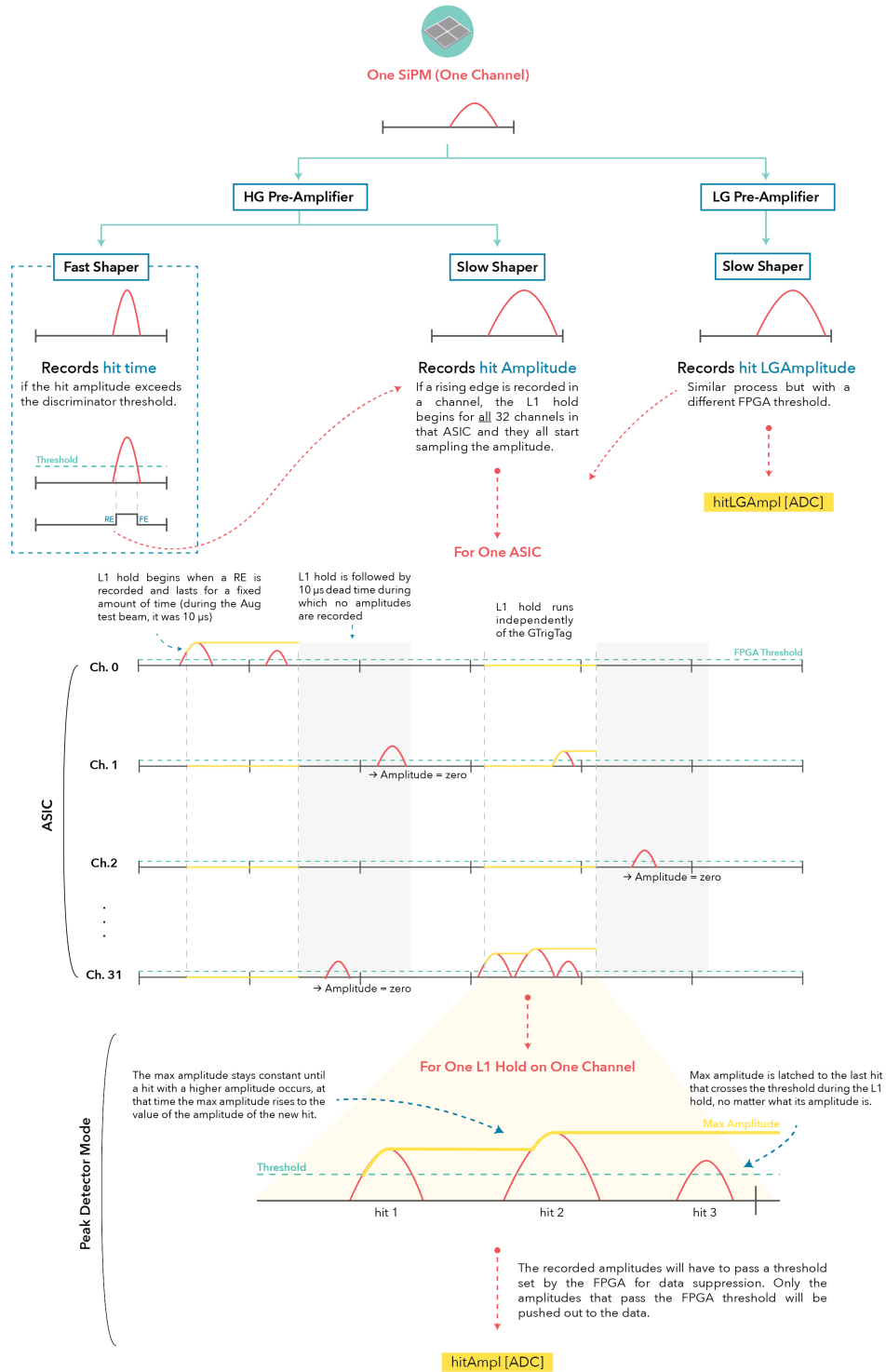


Figure 4.15.: The recorded amplitude information of a hit.

4.6.4. Data Structure

The DAQ produces four separate .daq files, one for each of the four MCRs. In order to read and analyze the data, these files must be unpacked and converted into a ROOT^[29] file with easy access to all hit information.

The first step in unpacking the data into a readable format is to unpack each MCR.daq file into 4 or 5 .daq files, one for each of the Front-end Boards in that Minicrate. These files are then sequentially read by the unpacking code that goes spill by spill to extract all information recorded by the electronics for each hit on the basis of 4-bit headers describing contents of 32-bit words. This information is then stored in separate ROOT trees for each FEB. In the case where no rising edge is recorded for a certain hit, the unpacking code would not push that hit's information to the output file.

The resulting ROOT file contains 19 trees that correspond to the 19 FEBs of the SuperFGD prototype. In order to read these files, one would need to loop over all trees and select all hits that occur within a certain time window with respect to the external trigger. Since this process was time consuming, a new data structure based on *hit* and *event* classes was developed.

In the conversion to the new data structure, the following definitions were used:

- **A Hit** - A signal recorded by one channel in one FEB, it has two coordinates determined by the side of the detector the FEB reads from.
- **An Event** - A group of hits from all FEBs occurring in the same GTrigTag, triggered by a signal on FEB 12.

Using these definitions, for each trigger from FEB 12 an event is created. This event is composed of all the hits that occur in the same GTrigTag as the trigger (i.e. within the same 10 μ s period of the global trigger clock). A more restrictive time window is left to be implemented during the analysis stage.

4.6.5. Calibration

The readout electronics of the SuperFGD output three different signal paths for the amplitude, the two digitized 12-bit high gain and low gain signals, and the Time-over-Threshold (ToT) signal obtained from the difference between the rising and falling edges recorded by the CITIROC. These three paths are calibrated and then combined, with some conditions, to create one amplitude that is mainly used in the analysis of the data; the hit charge.

1. Calibration of the HG signal

Using LED signals and the output charge distribution (in ADC units) of each channel in the detector, the ratio ADC/p.e. was calculated. This ratio represents

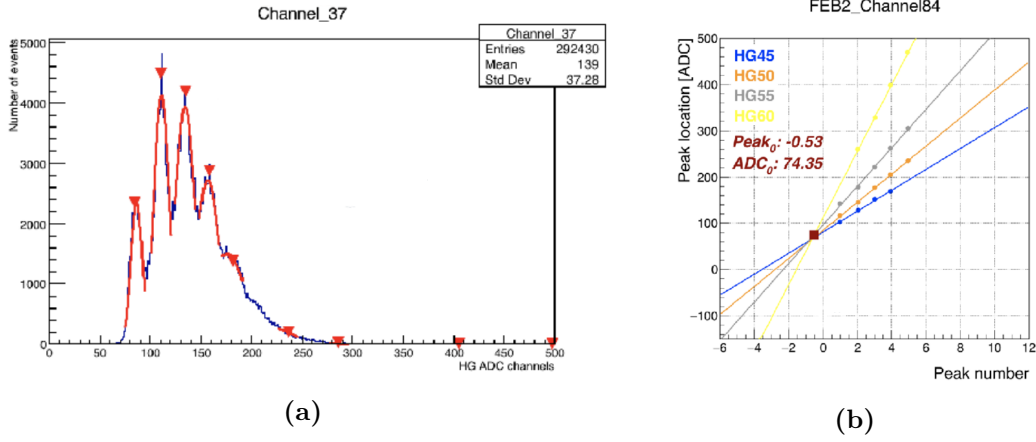


Figure 4.16.: (a) Output charge distribution produced by LED signals for one channel. (b) Peak location versus peak number for different HG settings.

the gain in ADC for each pixel fired in the MPPC. An example of such a distribution is shown in figure 4.16 (a). The first peak on the left corresponds to the case where no pixels are fired. The recorded signal, in this case, is caused by the electronic noise in the setup. The next peak is the case where one pixel is fired, and the third peak is when two pixels on the MPPC are fired. A clear separation between the peaks is an indication of a good photon counting capability for the MPPC.

By extracting the location of each peak (in ADC) and plotting it versus the number of the peak, one can extract the gain of the channel from the slope of the fitted line. For the SuperFGD prototype beam test, different HG and LG settings were used and therefore different sets of calibration parameters are needed to be produced. Figure 4.16 (b) shows the plot of the peak location versus the peak number for different settings of HG. The point where the four lines meet corresponds to the value of the pedestal.

2. Calibration of the LG signal

The LG signal is plotted against the HG signal to extract the LG calibration parameters for each channel. Figure 4.17 shows an example of such a plot using data from the beam test. The two signals are expected to be proportional, therefore the first part of the plot is linear. However, at a certain point the HG signal reaches saturation and the ratio LG/HG rises very quickly.

By fitting the linear region of the plot, one can extract the parameters that convert a LG signal to a corresponding HG signal for each channel, and for each HG and LG setting.

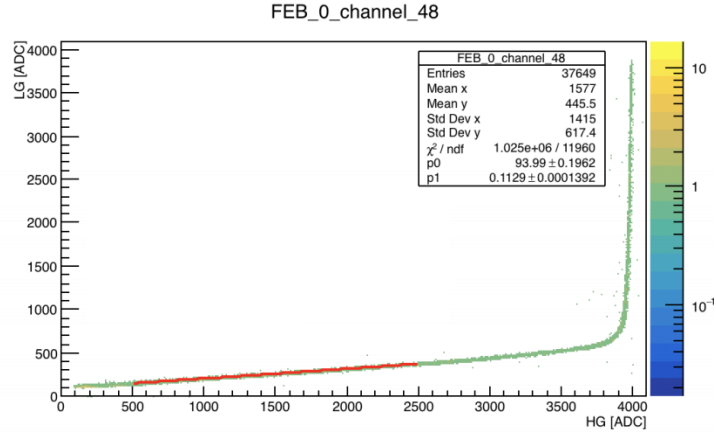


Figure 4.17.: A plot of LG versus HG signals using beam test data.

3. Calibration of the ToT signal

The ToT signal is sampled by the FPGA at a rate of 400 MHz, which corresponds to a point every 2.5 ns. The calibration parameters are extracted independently for the ToT→HG and ToT→LG calibrations. In both cases, the HG (or LG signal) is plotted against the ToT signal resulting in a plot that can be fitted using a polynomial function of the fifth order. The parameters of this fit are extracted for each channel separately and are used to perform the ToT→HG and ToT→LG calibrations.

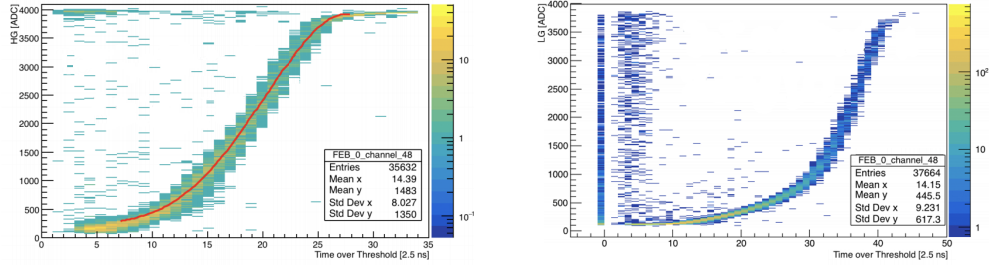


Figure 4.18.: A plot of HG versus ToT (left) and LG versus ToT (right) for the same channel using beam data.

The extracted parameters for the three signals are then used to convert the amplitude from units of ADC (or time) to units of photoelectrons (p.e.). In the case of the HG signal, the gain and the pedestal values are directly used to do the conversion according to the following formula:

$$HG [p.e.] = \frac{HG [ADC] - Pedestal [ADC]}{Gain [ADC/p.e.]} \quad (4.4)$$

For the LG signal, the calibration is done in two steps. First, the LG signal is converted to a HG signal, then the HG signal is converted to units of p.e. as explained above. This can be summarized as $\text{LG} \rightarrow \text{HG}[\text{ADC}] \rightarrow \text{HG}[\text{p.e.}]$. As for the ToT signal, if $\text{ToT} < 20$ [2.5 ns], first the calibration $\text{ToT} \rightarrow \text{HG}$ is performed using the extracted parameters of the fifth order polynomial, then the HG is converted to units of p.e. ($\text{ToT} \rightarrow \text{HG}[\text{ADC}] \rightarrow \text{HG}[\text{p.e.}]$). The $\text{ToT} \rightarrow \text{LG}[\text{ADC}] \rightarrow \text{HG}[\text{ADC}] \rightarrow \text{HG}[\text{p.e.}]$ calibration is used if $20 \leq \text{ToT} < 100$ [2.5 ns]. Values of ToT outside this range are considered unphysical and are assigned a reference value of -1 p.e.

Finally, the three resulting values of the amplitude in p.e. are combined to create one value that is referred to as the hit *charge*. To create this value, the charge of the hit is considered equal to the HG signal if the HG signal exists and is below saturation[§]. If the HG signal fails one or both of these conditions, the hit charge is equal to the LG signal (also if it exists and is below saturation). Otherwise, the ToT signal is used for the hit charge. The analysis of the data in this study is done using the hit charge for the amplitude.

[§]According to figure 4.17, the HG signal reaches saturation around 3800 ADC for that particular channel. Therefore, a common value of 3000 ADC is used as the maximum accepted amplitude, for all channels, while creating the hit charge.

*The task is not to see what has never been seen before,
but to think what has never been thought before about
what you see everyday.*

— Erwin Schrodinger

5

The Beam Test

Contents

5.1. The T9 Beam Environment	40
5.2. Test Setup	41

The SuperFGD prototype has been tested in the T9 beam environment at CERN for two periods in the summer of 2018. The first test period was between the 27th of June and the 11th of July, and the second was between the 22nd of August and the 5th of September. In the August/September test beam the TPC was included and positioned on the beam line. Data from the second test beam is better calibrated and therefore it was used for this study.

5.1. The T9 Beam Environment

T9 is a beam line in the CERN PS (Proton Synchrotron) east area secondary beam facility. In the east area, four beam lines (T8, T9, T10 and T11) are derived from the 24 GeV/c primary beam from the PS, which provides 2.4 second cycles with a flat top of about 400 msec^[24].

The proton beam from the PS accelerator is directed towards the north target. Upon collision with the target, different particles like electrons, protons, pions and muons (from pion decays) are produced. The T9 beam delivers these secondary particles at a production angle of 0 degrees with momenta between 0.5 GeV/c and 10 GeV/c and a theoretical momentum resolution of 0.24%^[25].

The north target contains 5 heads made of different materials and thicknesses, these targets are detailed in table 5.1.

Table 5.1.: The North target different head characteristics^[26].

Target no.	Material and Thickness	Diameter	Comments
1	200 mm Be + 3 mm W	10 mm	Electron Target
2	100 mm Al + 3 mm W	10 mm	Electron Target
3	200 mm Al	10 mm	Hadron Target
4	0 mm	-	Empty Target
5	20 mm Al	10 mm	Electron Target

During the SuperFGD beam tests, the 200 mm Aluminium target head was used.

After impinging on the target, the beam travels approximately 55 m before it enters the experimental area. Along the beam line, there is a set of optical devices composed of collimators and magnets that are used to control the beam. Dipole magnets are used to bend the beam and control its direction, while quadrupole magnets are used to focus it. The settings for these magnets are set by adjusting their currents through the computer in the T9 control room.

There are also two stoppers placed in order to block the beam in case someone needed to enter the area. When selecting a hadron beam, the two stoppers are moved out of the beam line, and the horizontal and vertical collimators are set to narrow settings (5 mm \times 5 mm or 5 mm \times 10 mm) to obtain a good momentum resolution for the beam. On the other hand, for a muon beam one stopper is kept in such that it would prevent particles other than muons from passing through to the experimental area. The collimator settings in this case are chosen to be wider (30 mm \times 30 mm) so that a higher particle rate can be achieved.

A simulation of the composition of the resulting beam as a function of the beam momentum for an electron-enriched target is shown in figure 5.1. This distribution is created at the position of the primary target, before pions get the chance to decay, which explains the absence of muons. When using a hadron target, the fractions of electrons and positrons will be heavily reduced^[27].

5.2. Test Setup

The SuperFGD prototype was placed along the beam line, 15 m away from the beam source. The MNP17 dipole magnet was used to produce a uniform magnetic field along the X axis of the detector. The field strength was set to 0.2 T for most of the test, it was occasionally raised to 0.7 T for some runs and up to 1 T for the photon beam runs.

The Aug/Sep beam test setup in the T9 area is shown in figure 5.2. The SuperFGD and the TPC were tested simultaneously during this test period.

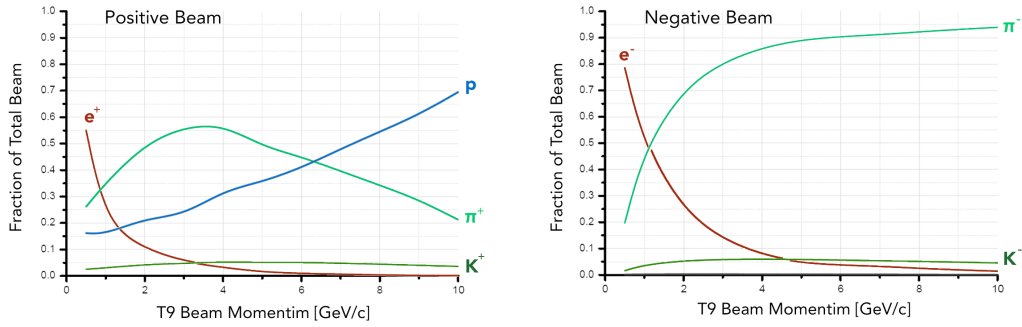


Figure 5.1.: Simulations of the T9 beam composition for an electron enriched target at the position of the primary target^[27].

The elements inserted along the beam line include^[3]:

1. Time-of-flight counters, used for particle identification, and also serve as a trigger for the SuperFGD events.
2. Lead degraders of 50-100 mm thickness, used during a few dedicated runs to impede the muons in order to obtain stopping muon data.
3. An MDX dipole magnet, used to deflect the charged particle beam during the photon beam runs.

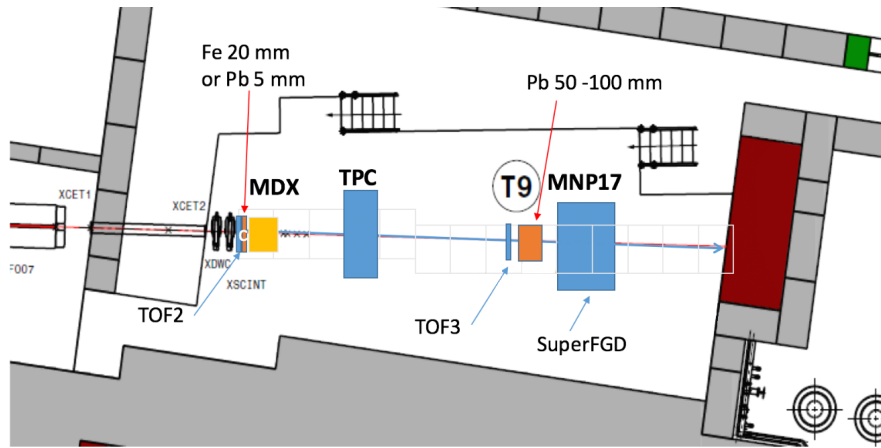


Figure 5.2.: The T9 area layout during the test^[3].

The data collected during the beam test include both hadron and muon runs. Several runs were obtained for momenta between 0.5 GeV/c and 2 GeV/c. The data also include a few photon beam runs.

*Science is different to all the other systems
of thought, because you do not need faith in it.
You can check that it works.*

— Brian Cox

6

Simulation of the SuperFGD

Contents

6.1. Simulation of the Detector Geometry	44
6.2. Simulation of the Detector Response	44
6.3. Creating Simulations for the SuperFGD Prototype	45

The ND280 upgrade simulation group has created simulations for the SuperFGD within the upgraded ND280 framework. The detector geometry and the particle trajectory in the detector are simulated by GEANT4, whereas neutrino interactions are simulated using GENIE. Figure 6.1 shows a GEANT4 rendering of the upgraded ND280 simulation.

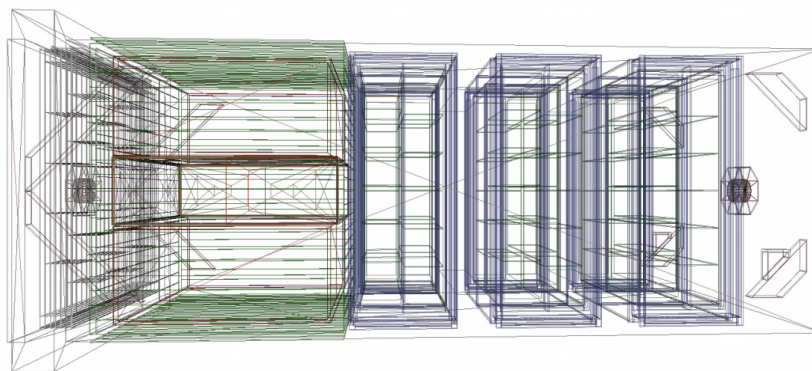


Figure 6.1.: A GEANT4 rendering of the Monte Carlo simulation^[3].

6.1. Simulation of the Detector Geometry

The geometry of the SuperFGD is simulated in GEANT4 by creating replicas of the $10 \times 10 \times 10 \text{ mm}^3$ cubes. Each cube has three holes with a radius of 0.75 mm whose centers are positioned 3 mm from the cube edge, these holes are removed from the volume of the cube and are filled with 0.5 mm radius fibers. The reflective coating is also simulated by subtracting the 0.1 mm coating thickness from the 10 mm edge of the cube^[3]. Figure 6.2 shows the simulated SuperFGD cube.

The material used for the cubes and the coating is Polystyrene $\text{C}_6\text{H}_5\text{CH}-\text{CH}_2$ (C_8H_8). The plastic scintillator material of the SuperFGD cubes is set as the sensitive material in the GEANT4 simulation, i.e. only the energy deposited in this material is recorded. Therefore, the coating and fibers are considered dead volume.

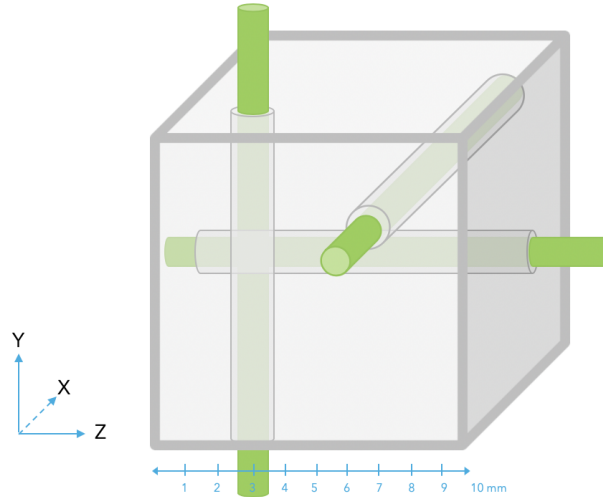


Figure 6.2.: The simulated SuperFGD cube.

To construct the SuperFGD, a detector with the dimensions of $1920 \times 1920 \times 560 \text{ mm}^3$ is created from these cubes. All cubes are identical in the simulation, and no gaps are introduced between adjacent cubes.

6.2. Simulation of the Detector Response

In order to simulate some aspects of the detector response, several effects need to be taken into account and applied to the GEANT4 output. These effects include the response of the plastic scintillator (e.g. saturation effects), the response of the fibers (e.g. attenuation), and the response of the MPPCs.

The parameters used to introduce these effects to the simulations were extracted from the current FGDs or from the beam tests of the SuperFGD prototypes.

To estimate the fraction of deposited energy that is emitted as scintillation light, Birk's equation (6.1) was used with a value of 0.0208 cm/MeV for Birk's constant.

$$E_{sci} = \frac{E_{dep}}{1 + K_B \frac{dE}{dx}} \quad (6.1)$$

In order to convert this energy into a number of photoelectrons, the number of photons emitted per MeV of scintillation energy is required. According to measurements in the FGD, this number is 156.42 γ /MeV. However, further calibration of this value is required for more accurate results.

The next applied response is the light attenuation in the fibers, applied using the relation in equation 6.2. The constants in the equation are based on measurements in the FGD with the same type of WLS fibers used in the SuperFGD.

$$E_{attenuated} = E \times \left[A e^{(-x-d)/L} + (1 - A) e^{(-x-d)/S} \right] \quad (6.2)$$

The delay in the fibers is also accounted for by adding the transition time of light in the fiber which is equal to the distance travelled in the fiber divided by the speed of light.

Finally, a photon detection efficiency (PDE) of 35% is taken into account for the MPPCs.

6.3. Creating Simulations for the SuperFGD Prototype

For the purposes of this study, a modified version of this framework was used in order to obtain simulations with similar conditions to the SuperFGD prototype. These modifications include disabling all other detectors within the ND280, modifying the size of the SuperFGD to 240×80×480 mm³, and using a particle gun as a beam source instead of an input from GENIE.

In all simulations, a proton particle gun is used as the generator with an initial position at the center of the cube with XY coordinates of (13,5). In order to obtain a more realistic beam, a Gaussian variation is introduced to the position of the particle gun with a standard deviation of 4 cm in the X direction and 2 cm in the Y direction.

All cubes were constructed with a cube edge of 10 mm and a coating thickness of 0.1 mm.

*No great discovery was ever made
without a bold guess.*

— Isaac Newton

7

Stopping Proton Studies

Contents

7.1. Motivation to Study Stopping Protons	47
7.2. Samples of Stopping Protons	47
7.2.1. Beam Test Data and Data Quality	47
7.2.2. SuperFGD Proton Beam Simulations	48
7.2.3. Event Selection	49
7.3. Event Displays	52
7.4. Part 1: Selection of Simulation Sample	53
7.4.1. The Range of Protons in the SuperFGD	53
7.4.2. Beam Momentum Analysis	58
7.5. Part 2: Beam Test Data vs. Simulation Analysis	62
7.5.1. Obtaining the dE/dz Curves	62
7.5.2. dE/dz Comparison	64
7.5.3. Fiber Response Comparison	68
7.5.3.1. Attenuation	68
7.5.3.2. Energy Deposition	69
7.6. Effect of Cube Coating, Holes and Fibers(From Simulations) 72	

For the purposes of this study, a proton beam run is chosen from the beam test data and simulations of the SuperFGD with proton beams of several values of momenta are created. The first step in this analysis is to select samples of stopping proton events. The event selection procedure is explained in section 7.2.3.

This analysis is divided into two parts. Part 1 concentrates on finding the correct simulation for a fair comparison with the beam test data. This comparison is then carried out in part 2.

7.1. Motivation to Study Stopping Protons

Stopping proton studies provide a great tool to understand the response of the detector for large energy deposition. At the stopping point, the proton deposits a large amount of energy in a small volume. This large value of dE/dx can be used to study crosstalk*, MPPC and scintillator saturation, and quenching effects.

As explained in section 3.2, protons passing in a material may undergo nuclear interactions causing them to scatter or produce secondaries. These interactions do not obey a simple theory and must be properly identified to extract their cross sections. Since the probability of interaction increases as a proton slows down, the stopping point of the proton may exhibit a higher number of nuclear interactions. Obtaining a sample of stopping proton events provides the first step for future studies into these interactions.

In the case of neutrino experiments, proton detection is an important aspect of characterizing neutrino interactions. As discussed in section 2.3, neutrinos may interact with neutrons in the detector creating a lepton and a proton. Therefore, observing this CCQE interaction requires efficient proton detection.

This study provides the first phase of analysis aiming to determine the appropriate selection criteria to isolate samples of stopping proton events. It also investigates the proper simulation parameters that must be used to obtain simulations that can be compared with real data to perform more in depth studies.

7.2. Samples of Stopping Protons

7.2.1. Beam Test Data and Data Quality

During the analysis phase, some issues were discovered in the beam test data files. An example of such issues is the presence of hits for which no falling time was recorded, causing the computation of a negative Time-over-Threshold. The origin of the problem was found to be due to a FIFO (First In, First Out) that was getting full causing the mis-assignment of falling times to rising times. A simple fix to this problem was done by increasing the memory of the FIFO to accommodate for the cases when a large number of channels receive a signal in a short period of time on one FIFO. As for now, hits with missing falling times are assigned a charge of -1 p.e. to distinguish them from the rest.

Another issue that was also observed in some runs was that certain FEBs went out of synchronization with the other FEBs causing discrepancies in the recorded time of each event. This problem can be seen in the event displays when there are persistent gaps throughout the data in the cells corresponding to one or more FEBs, as shown in figure 7.1. The cause of this issue was determined to be a faulty channel on the synchronisation fanout board which has since been replaced.

*The fraction of scintillation light that may leak from one cube to neighbouring ones.

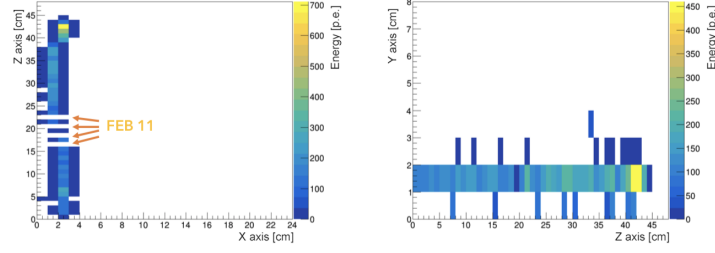


Figure 7.1.: An event display showing the top view (left) and side view (right) of a proton track for a data run where FEB 11 went out of synchronization.

Finally, some noise affecting the output of the detector during the beam test was discovered. This noise appears in the event displays as systematic lines with equal distances suggesting it might be an electronic noise. However, the source of the noise has not been conclusively determined. Figure 7.2 shows an example of such event.

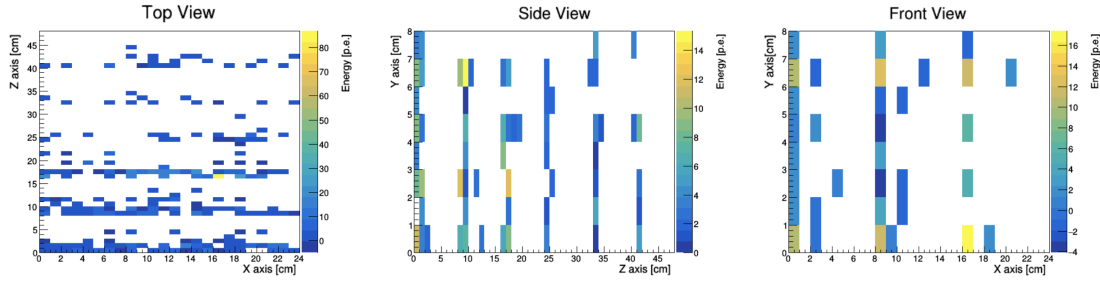


Figure 7.2.: A noisy event from the beam test data.

These issues severely limit the number of data runs that can be used in the analysis. The data used in this study is from a 30-minute run with an 800 MeV/c proton beam. During the run, the MNP17 magnet was on and set to a current of 135 A, which corresponds to a magnetic field of 0.2 T along the X axis of the detector.

7.2.2. SuperFGD Proton Beam Simulations

In order to study stopping protons using the Monte Carlo, five runs were simulated with beam momenta between 700 and 800 MeV/c (in steps of 25 MeV/c) and a magnetic field of 0.2 T along the X axis. Each simulation consists of a total of 20,000 events.

In section 7.6, a small study is made to investigate the effects of simulating the cube coating and WLS fibers as dead volume in the SuperFGD. For the purpose of this study, four additional simulations were created with beam momenta of 700 and 750 MeV/c. Table 7.1 shows a summary of all simulations.

Table 7.1.: List of all created simulations.

P [MeV/c]	Coating [mm]	Hole r [mm]	Fiber r [mm]
800	0.1	0.75	0.5
775	0.1	0.75	0.5
750	0.1	0.75	0.5
725	0.1	0.75	0.5
700	0.1	0.75	0.5
750	0.0	0.75	0.5
700	0.0	0.75	0.5
750	0.0	0.0	0.0
700	0.0	0.0	0.0

7.2.3. Event Selection

To select a sample of stopping proton events from the beam test data, the first step is to apply a time window on the group of hits that belong to each event in order to reduce the amount of noise and background. The main source of this background is cosmic ray particles that may enter and interact with the SuperFGD at any time. Since such background is not present in the simulations, this step is not required for the MC analysis.

The time window is based on the time difference between the arrival of the particle to the trigger[†] (trigger time) and the recording of the hit in the detector (hit time).

Despite the fact that the trigger time occurs earlier than the hit time, the registered trigger time has a larger value than the registered hit time. The reason for this is that the signal from the trigger is delayed significantly while travelling across the >5 m long cables used during the beam test. This causes the value of ($\Delta t = \text{hit time} - \text{trigger time}$) to be negative.

Figure 7.3 shows the distribution of Δt for all hits in the run data. According to this distribution, a time window of (-80, -60) time units (time unit = 2.5 ns) was applied to the hits throughout this study. This time window is equivalent to 50 ns.

In order to select a sample of stopping proton events, careful criteria must be considered. A stopping proton must be completely contained within the volume of the SuperFGD. It is expected to deposit a large amount of energy at its stopping point, some of which may leak to neighbouring cubes in the form of crosstalk. To make the analysis easier, events with multiple tracks are eliminated.

[†] A scintillator Time-of-Flight detector used as an external trigger to signal the arrival of a proton from the beam.

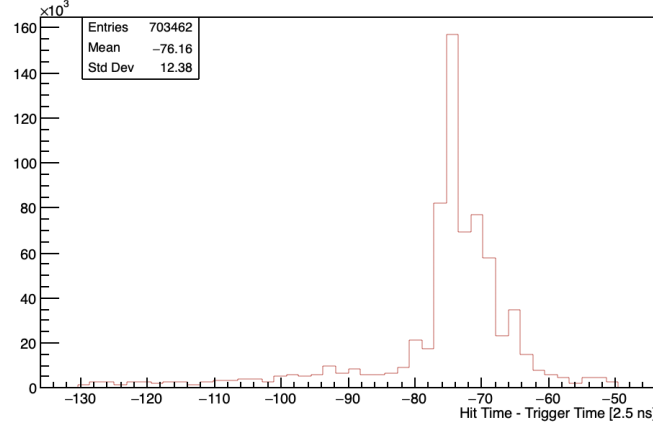


Figure 7.3.: Distribution of Δt for all hits in the run data.

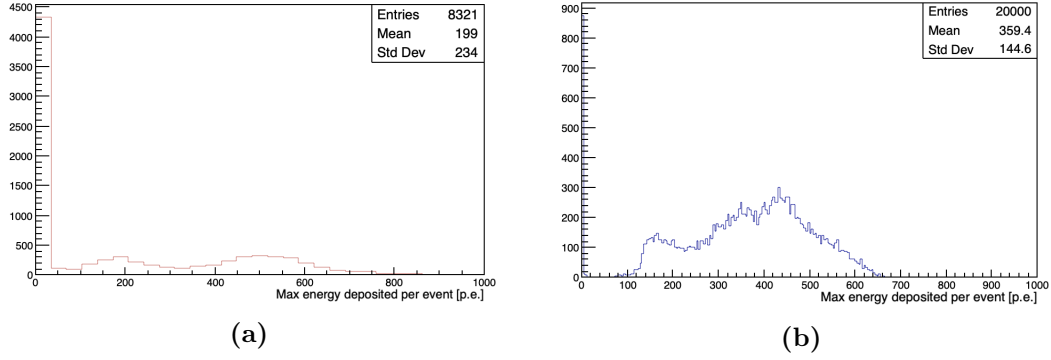


Figure 7.4.: The maximum energy deposited (in the horizontal fibers along the Y axis) in each event of the beam test data (a) and a simulation of 750 MeV/c (b).

The event selection criteria applied in this study, to both data and MC, are as follows:

1. Require that no energy is deposited in the last layer of the detector along the Z axis. This selection eliminates particles that do not stop in the detector.
2. Require that the maximum energy deposited in an event (in one fiber) must be above 125 p.e. This selection eliminates the noise mentioned in section 7.2.1. Figure 7.4 shows the distribution of the maximum energy deposited in each event of the beam test data and one simulation sample. According to the simulation, a proton track has a maximum energy deposition of at least 125 p.e. Therefore, this value was used as a threshold to eliminate the contamination of noisy events causing the peak at low energies in the beam test data.
3. Require that, for the front (XY) view, the standard deviation of the distribution of the position of hits in both X and Y must be below 1.0. This selection limits the number of events with two or more proton tracks. Figure 7.5 shows the front view for an event with one proton track compared to that of an event with two tracks.

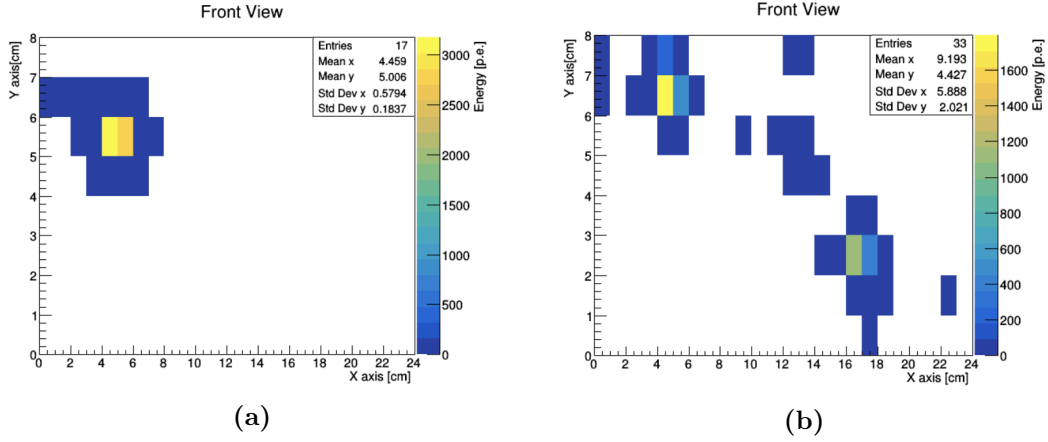


Figure 7.5.: (a) The front (XY) view for an event with one proton track. (b) The front (XY) view for an event with two proton tracks.

Since stopping protons tend to have straight tracks with minimum scattering, the front view is expected to consist of one or two points with high energy deposition (corresponding to the main track) surrounded by low energy crosstalk. Therefore, the standard deviation along the X and Y directions is expected to be below 1.0.

4. Allow a maximum of 2 layers with zero deposited energy along the proton's track. This selection eliminates events with many gaps which lead to inaccurate measurements of the energy deposition. A gap in a proton's track may occur if the proton travels between adjacent cubes, or through one of the holes.
5. Require that no energy is deposited in the outer layers of the detector along the X and Y axes. This selection eliminates particles that escape the detector and assures that the event is contained within the volume of the SuperFGD.

To estimate the efficiency of these cuts, table 7.2 shows the percentage of beam test events rejected with each cut. According to these results, the first and last cuts reject the highest number of events. Consequently, the low statistics are mainly due to the hard conditions on the outer layers of the detector, especially on the first and last layers in the Y axis which constitute 25% of the 8 Y layers.

Table 7.2.: The efficiency of the selection cuts for the beam test data.

Cut	Rejected%
Cut 1	62.5%
Cut 2	11.2%
Cut 3	28.7%
Cut 4	31.4%
Cut 5	54.5%

In the case of the simulations, these statistics can be significantly increased by setting a constant entry position for the particle gun at the center of the detector. However, adding variation to the entry position is more realistic and in agreement with the T9 test beam.

After applying these conditions, table 7.3 shows the samples of stopping proton events obtained from all MC and beam test data files.

Table 7.3.: Details of all data.

P [MeV/c]	Total Events	Selected Events
800 Data	8,321	616
800 MC	20,000	29
775 MC	20,000	244
750 MC	20,000	414
725 MC	20,000	604
700 MC	20,000	945

As shown in the table, the sample of 800 MeV/c stopping proton events that passed the event selection in the simulation is very small compared to the beam test data. The reasons for this will be investigated in this study.

7.3. Event Displays

Using a hit's amplitude and the channel location in the detector, it is possible to create simple event displays for the selected stopping proton events.

Projected 2-dimensional event displays for the SuperFGD are created using signals from the fibers that are along the third dimension (perpendicular to the view). The front (XY) view is constructed using the horizontal fibers along the Z axis, the side (ZY) view uses the horizontal fibers along the X axis and the top (XZ) view uses the vertical fibers along the Y axis.

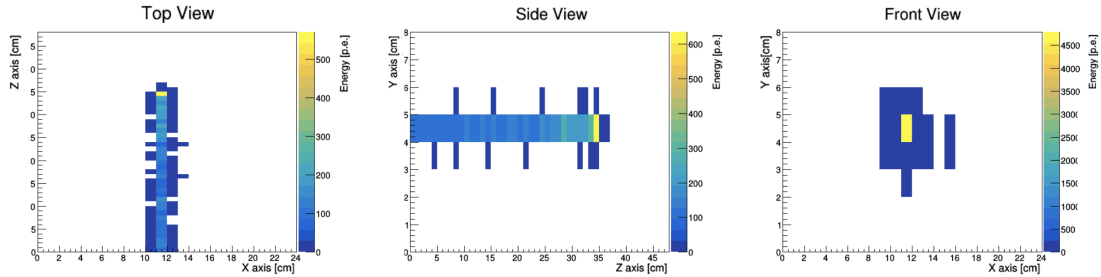


Figure 7.6.: A stopping proton event from the beam test data.

Figure 7.6 shows an example of an event display from the beam test data. The views show the proton track and the large energy deposition at the stopping point, as well as the optical crosstalk on each side of the proton path.

By comparing the top and side views, it is clear that the amount of horizontal crosstalk is significantly larger than the vertical crosstalk. This is mostly due to the Tyvek reflector layers used between the horizontal planes of cubes in the prototype, which limit the amount of light leaking vertically to other cubes.

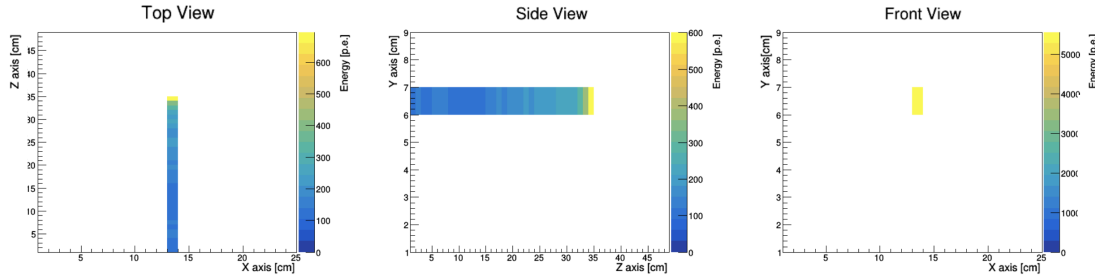


Figure 7.7.: A stopping proton event from a 700 MeV/c simulation.

Similarly, event displays were constructed for the simulations. Figure 7.7 shows an event display for a 700 MeV/c proton beam MC event. Since crosstalk was not simulated in this study, the event displays for the MC are cleaner compared to those observed in the data. Appendix B shows a random sample of stopping proton events from the beam test and simulations.

7.4. Part 1: Selection of Simulation Sample

One of the 5 simulations must be chosen in order to perform a fair comparison with the beam test data. The right simulation is selected based on two criteria; the range of the protons in the SuperFGD, and the momentum of the protons just before they enter the detector. The latter is calculated by reconstructing the beam momentum from the sample of stopping proton events, which is possible since stopping protons are contained in the detector and the event selection guarantees that they deposit all their energy inside it.

7.4.1. The Range of Protons in the SuperFGD

The range of the proton in the SuperFGD is initially determined to be equal to the distance it travels up to the cell with the maximum energy deposition, where it is thought to stop. Figure 7.8 shows the range of the selected sample of beam test stopping protons according to this definition. The figure shows an average range of 41.59 ± 0.21 cm.

In order to investigate the possibility that the cell with the maximum energy deposition is not always the stopping point of the proton, one approach is to look at the amount of energy deposited in the following cube, as shown in figure 7.9.

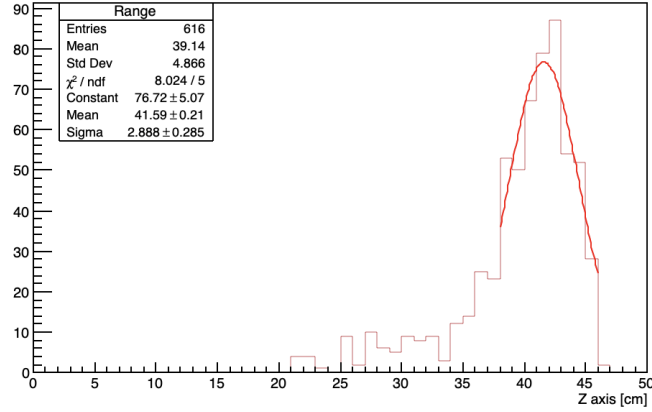


Figure 7.8.: The range of the beam test protons in the SuperFGD, where the range is simply defined as the distance up to the cell of maximum energy deposition.

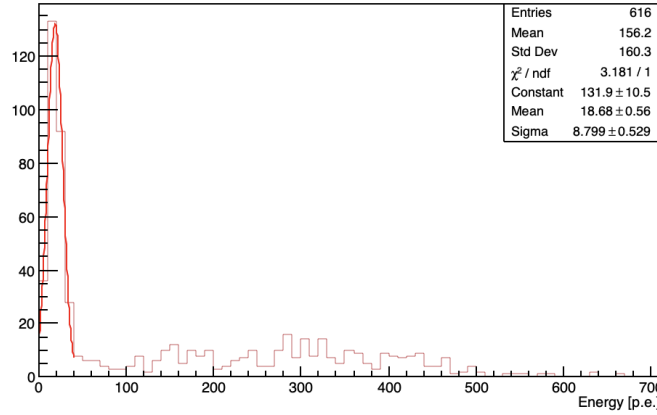


Figure 7.9.: The distribution of the energy deposited in the cube following the one with maximum energy deposition for the beam test sample.

In all cases, a fraction of the light from the stopping point is expected to leak into the following cube in the form of crosstalk. For the SuperFGD cubes, this fraction is estimated to be around 3.7%^[3]. To determine the amount of energy that is expected as crosstalk from the cell with the maximum energy deposition, the distribution of the maximum energy in each event of the sample is used.

According to figure 7.10, the mean maximum energy deposited in a stopping proton event in one fiber is 474.3 ± 5.3 p.e. Using this value, a 3.7% crosstalk corresponds to 17.5 p.e. which explains the peak in figure 7.9 at low depositions.

On the other hand, figure 7.9 shows a significant number of events where the cube following the one with the maximum energy deposition sees energy depositions of over 100 p.e. A sketch for such an event is shown in figure 7.11.

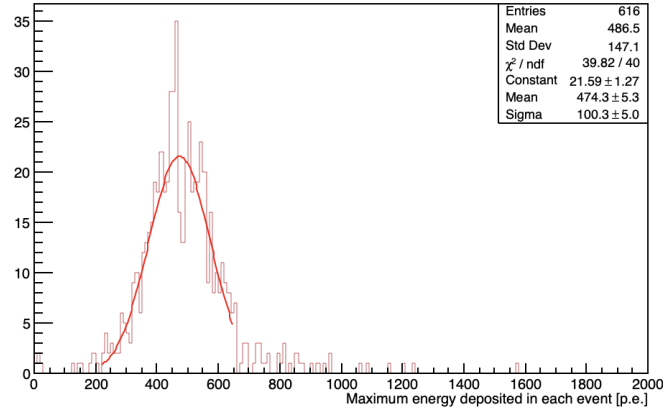


Figure 7.10.: The distribution of the maximum energy deposited in each event of the beam test sample.

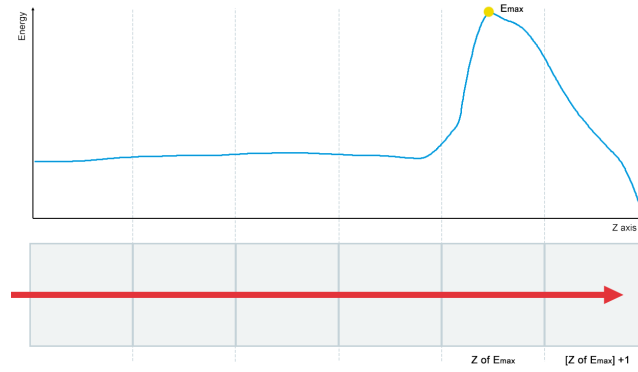


Figure 7.11.: A sketch of a proton track showing the cubes and the energy deposition.

Taking that into account, the range of the proton is redefined such that:

- The range is equal to the value along the Z axis at which maximum energy deposition (E_{max}) occurs, only if the energy deposition in the next cube is below 50% of E_{max} .
- If the energy deposition in the next cube is above 50% of E_{max} , the range equals the distance along the Z axis to that cube (i.e. previously defined range +1 cm).

After applying this condition, the mean range of the sample slightly increased to 42.06 ± 0.17 cm as seen in figure 7.12 (a). Figure 7.12 (b) shows the energy deposited in the following cube where a smaller number of high energy depositions is observed.

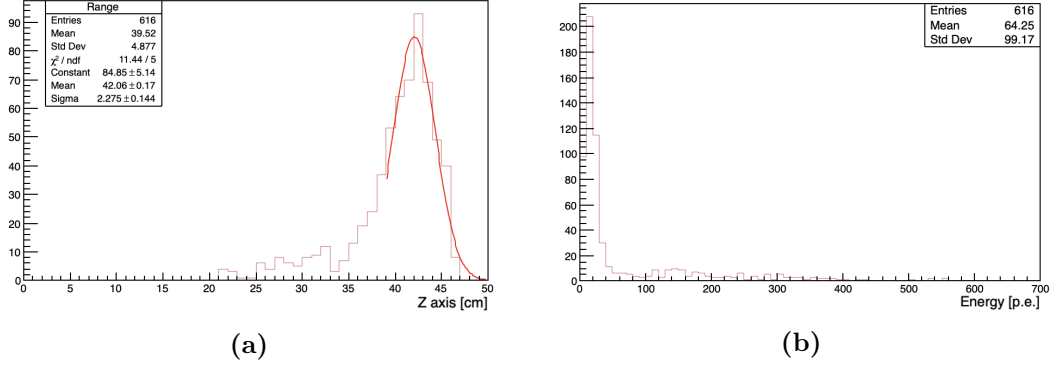


Figure 7.12.: (a) The range distribution after applying the new condition. (b) The distribution of energy deposited in the cube following the one with the maximum energy deposition, after the range redefinition for the beam test sample.

The same range definition was applied to the simulations. Figure 7.13 shows the range distribution along with the distribution of the energy deposited in the cube following the one with the maximum energy deposition for the 5 samples of MC stopping protons.

Table 7.4 shows a summary of the mean range observed for each value of the beam momentum, for both data and simulations.

Table 7.4.: Mean ranges for all stopping proton samples.

P [MeV/c]	Mean Range [cm]
800 Data	42.06 ± 0.17
800 MC	Fit fails (low statistics)
775 MC	46.44 ± 0.08
750 MC	42.29 ± 0.06
725 MC	38.3 ± 0.0
700 MC	34.44 ± 0.03

According to the range analysis results, it is evident that the simulations with 800 MeV/c momentum has very low statistics indicating that the protons do not stop within the volume of the detector. On the other hand, the beam test sample has a mean range of 42.06 ± 0.17 cm which is most comparable to the mean range of the simulation with momentum of 750 MeV/c.

Another difference between the beam test data and the simulations is that the width of the range distributions is larger in the case of the beam test sample. However, this can be justified knowing that the T9 beam is not completely monochromatic as the case for the particle gun used in the MC. A more realistic beam can be simulated by introducing a variation in the momentum of the particle gun.

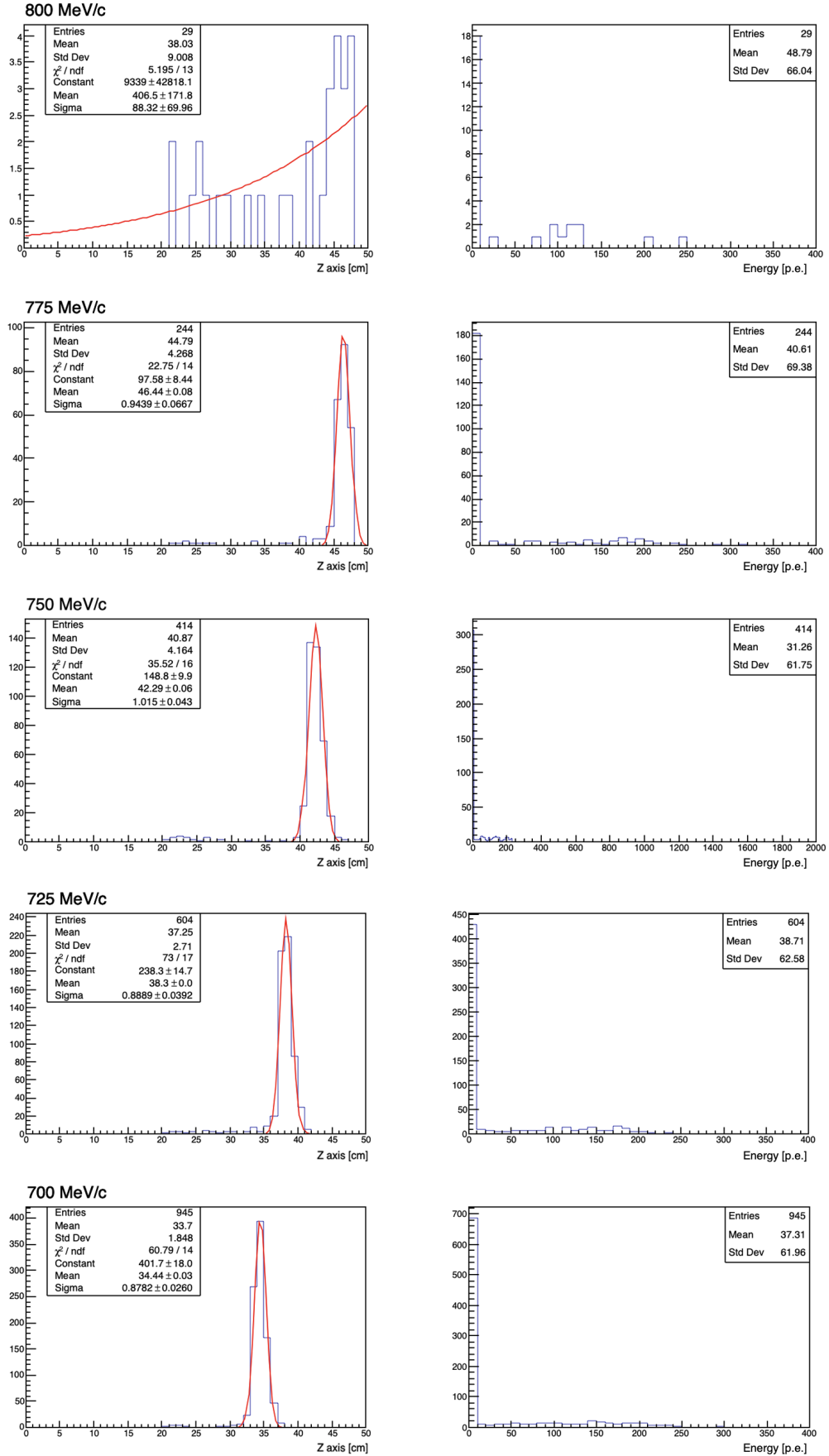


Figure 7.13.: The range and the distribution of the energy in the cube following the one with maximum energy deposition for the 5 samples of stopping proton simulations.

The dispersion of the T9 beam can be estimated using the results above for the beam test data and the simulation sample of 750 MeV/c, assuming that:

$$\sigma_{Data}^2 = \sigma_{Beam}^2 + \sigma_{MC}^2 \quad (7.1)$$

Where $\sigma_{Data} = 2.275$ and $\sigma_{MC} = 1.015$ (from figures 7.12 (a) and 7.13), and the beam dispersion is given by:

$$Beam\ dispersion = \frac{\sigma_{Beam}}{Range} = \frac{2.03}{42.29} = 0.048 \quad (7.2)$$

For an 800 MeV/c beam, a 4.8% dispersion corresponds to a window of ± 38.5 MeV/c.

7.4.2. Beam Momentum Analysis

Several factors may introduce a discrepancy between the value of the beam momentum set for the T9 beam during the beam test, and the momentum of the protons just before they enter the SuperFGD. These factors include the presence of the TPC and trigger scintillators along the beam line and before the SuperFGD, which contribute to some energy losses for incoming particles.

To investigate the previous observations of the large difference between the 800 MeV/c beam test results and the simulation with the same momentum, the momentum of the incoming protons was reconstructed from the selected stopping proton events using two methods; the kinetic energy of the protons, and their range into the SuperFGD.

1. Beam Momentum Reconstruction by Kinetic Energy

The total energy of a particle is the sum of its kinetic and rest mass energies. In natural units ($c = \hbar = 1$), it can be written as:

$$E_{tot} = KE + m = \sqrt{p^2 + m^2} \quad (7.3)$$

Where p is the momentum of the beam, and m is the mass of the proton ($m_p = 938.27$ MeV/ c^2 ^[10]). By summing the total energy deposition along the proton's track, we can obtain its kinetic energy which can then be used to reconstruct its momentum just before entering the SuperFGD using the relation:

$$p = \sqrt{(KE + m)^2 - m^2} \quad (7.4)$$

Figure 7.14 shows the distribution of the total energy deposited in the horizontal fibers for each event. The mean value extracted from the plot is around 6345 ± 30.1 p.e. The first step is to convert the energy from units of p.e. to units of MeV, which can be achieved using the following concepts:

1. 50 p.e. is approximately the energy of one minimum-ionizing particle (MIP) in one fiber, in one cube of the SuperFGD^[3].
2. A MIP deposits 2.05 MeV/cm in Polystyrene^[10].

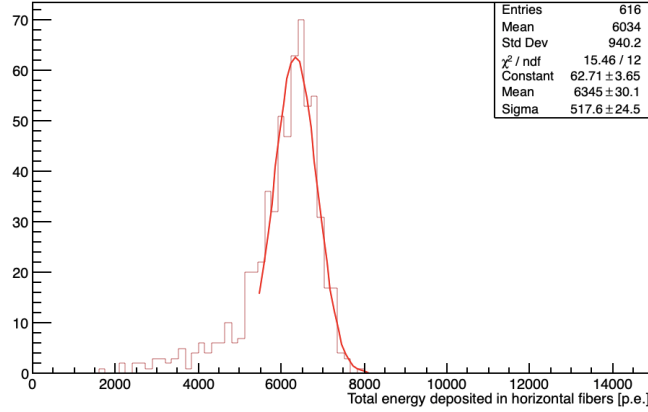


Figure 7.14.: The total energy deposited in the horizontal fibers for the beam test data.

The energy conversion can thus be applied through the following formula

$$E[MeV] = \frac{E[p.e.] \times 2.05[MeV/cm]}{50[p.e./cm]} \quad (7.5)$$

The mean kinetic energy of the sample is therefore calculated to be 260.15 ± 1.23 MeV. Using equation 7.4, the corresponding beam momentum is 745.47 ± 1.41 MeV/c which is significantly lower than the expected 800 MeV/c value set during the beam test.

This energy conversion is not required for the simulations since an output in MeV is already available. Due to the very low statistics of the 800 MeV/c simulation, it will no longer be used in the analysis. Figure 7.15 shows the total energy deposited in the horizontal fibers for each event, and for each value of the remaining samples.

Using equation 7.4, each value of the beam momenta was reconstructed. Table 7.5 shows the results for all samples[‡]. It is observed that the reconstructed momentum is always less than its true value. This observation, in the case of the beam test data, may be explained by energy losses prior to the protons' entry to the SuperFGD.

Despite the fact that the simulations do not account for such energy losses, an average difference of 18.69 MeV/c is observed between the true and reconstructed momenta. As explained in chapter 6, there are two sources of dead volume in the simulations of the SuperFGD; the cube coating and the WLS fibers. The effects of which are studied in section 7.6.

[‡]The uncertainty in the reconstructed momentum was calculated using the principle of error propagation, as explained in appendix A.1.

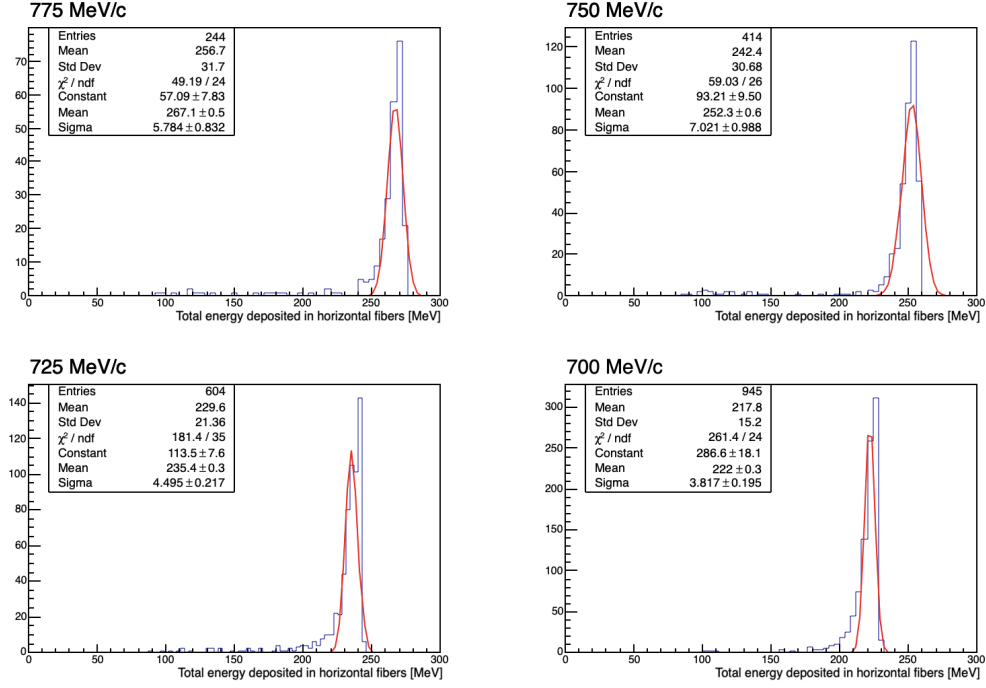


Figure 7.15.: The total energy deposited in the horizontal fibers for each of the MC.

Table 7.5.: Reconstructed momentum (by KE) for all stopping proton samples.

P [MeV/c]	Mean KE [MeV]	Recon. P [MeV/c]	ΔP [MeV/c]
800 Data	260.15 ± 1.23	745.47 ± 1.41	54.53 ± 1.41
775 MC	267.1 ± 0.5	756.58 ± 0.89	18.42 ± 0.89
750 MC	252.3 ± 0.6	732.78 ± 0.99	17.22 ± 0.99
725 MC	235.4 ± 0.3	705 ± 0.71	20 ± 0.71
700 MC	222 ± 0.3	682.46 ± 0.71	17.54 ± 0.71

2. Beam Momentum Reconstruction by Range

Separately, the range was also used to reconstruct the momentum and compare the results of both approaches. The range obtained from the selected events is compared against data from the PSTAR (Proton Stopping-Power and Range) database^[28] by the National Institute of Standards and Technology (NIST) for a Polystyrene scintillator to determine the momentum.

Figure 7.16 shows the relation between the kinetic energy and the range according to data from the PSTAR database. In this energy region, a polynomial of the second degree can be used as a good fit to extract the relationship between the kinetic energy (in MeV) and the range (in cm).

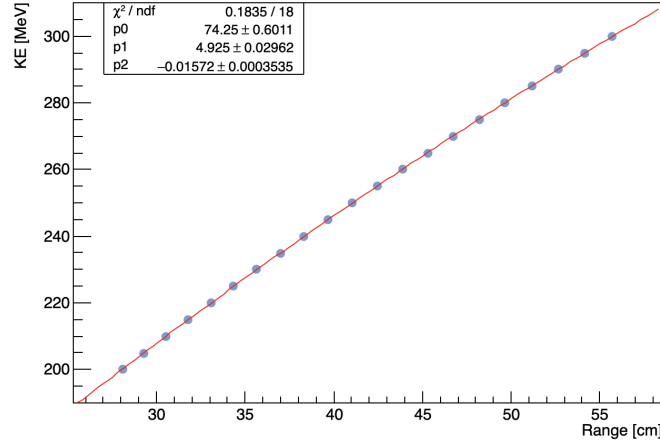


Figure 7.16.: The kinetic energy as a function of the range^[28].

Using the resulting fit parameters, the relationship can be written as:

$$KE(x) = 74.25 + 4.925x - 0.01572x^2 \quad (7.6)$$

Using this relationship and the ranges obtained for the samples (Table 7.4), the kinetic energy of each sample can be computed. This kinetic energy can then be used to reconstruct the momentum of the beam using equation 7.4. Table 7.6 shows the results of this procedure for all stopping proton samples[§].

Table 7.6.: Reconstructed momentum (by range) for all stopping proton samples.

P [MeV/c]	Mean Range [cm]	KE [MeV]	Recon P [MeV/c]	ΔP [MeV/c]
800 Data	42.06 ± 0.17	253.59 ± 0.61	734.89 ± 0.99	65.11 ± 0.99
775 MC	46.44 ± 0.08	269.06 ± 0.28	759.71 ± 0.67	15.29 ± 0.67
750 MC	42.29 ± 0.06	254.41 ± 0.22	736.21 ± 0.6	13.79 ± 0.6
725 MC	38.3 ± 0.0	239.81 ± 0.0	712.33 ± 0.0	12.67 ± 0.0
700 MC	34.44 ± 0.03	225.22 ± 0.12	687.92 ± 0.45	12.08 ± 0.45

According to table 7.6, the reconstructed momentum in this method is also below the true value for all samples. Since the reconstruction by range method is not directly affected by missing energy depositions in the detector, it is expected to be more accurate than the method of reconstruction by kinetic energy. In the case of the simulations, this can be observed by the decrease of the average difference (ΔP) between the reconstructed and true values of the momentum from 18.3 MeV (in the KE method) to 13.4 MeV/c.

[§]The uncertainty in the kinetic energy was calculated using the principle of error propagation, as explained in appendix A.2.

On the other hand, the beam test reconstructed momentum was less than the set value of 800 MeV/c by over 50 MeV/c in both reconstruction methods. This result, coupled with the previous observation for the range, points to the conclusion that the protons in the beam test sample have lower true momentum than 800 MeV/c and are more comparable to a simulation of 750 MeV/c. This conclusion is further strengthened by the fact that protons of 800 MeV/c momentum have a range of 54.18 cm in polystyrene^[28] and are, therefore, not expected to stop in the 48 cm long SuperFGD. Which explains the very low statistics of the 800 MeV/c simulation.

7.5. Part 2: Beam Test Data vs. Simulation Analysis

According to the analysis performed in part 1, the simulation sample of 750 MeV/c protons is selected for further comparisons with the beam test data. These comparisons include the dE/dz curves of the two samples as well as some fiber effects.

7.5.1. Obtaining the dE/dz Curves

The dE/dz curve of an event can be constructed using the total energy deposited in each 1 cm layer of the detector along its Z axis. Figure 7.17 shows an event display of a stopping proton event from the beam test data, along with the dE/dz curves obtained from the top and side views as well as the sum of the two.

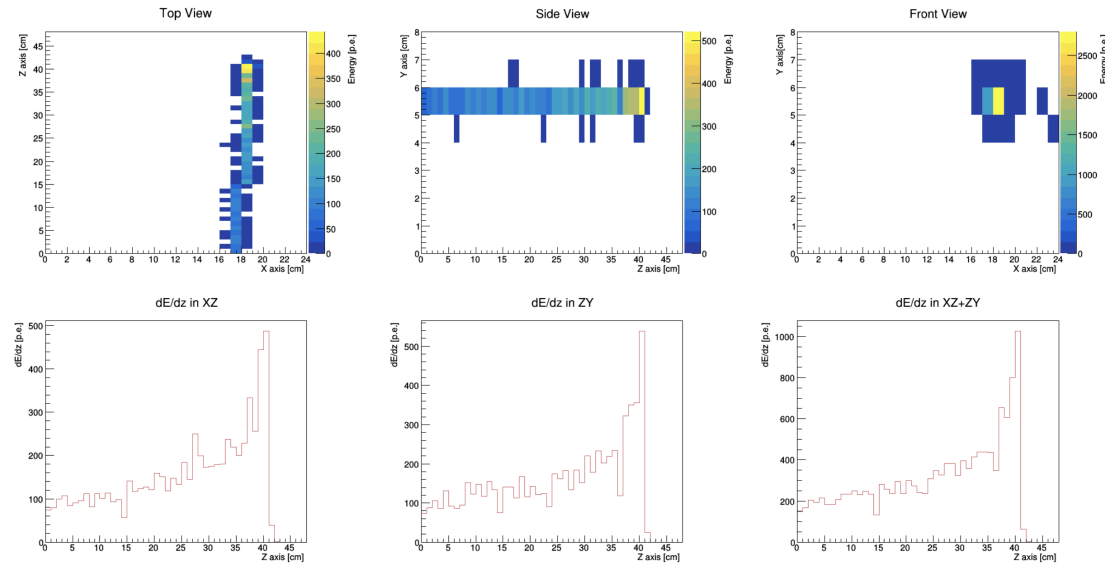


Figure 7.17.: A stopping proton event display from the beam test data along with the corresponding dE/dz curves.

Since the vertical fibers in the SuperFGD prototype are connected to three different types of MPPCs with different gain, the top (XZ) view is not used in this study. The following dE/dz analysis is performed using the side view obtained from the horizontal fibers along the X axis.

The total dE/dz curve of the sample is created from the sum of dE/dz curves of all selected events by finding the stopping point of the proton (as defined in section 7.4.1) and using it as a reference point to construct all points before and after it. Each bin in the curve is then normalized to the number of times it has been filled such that differences in the range of the protons between different events would be taken into account. The dE/dz curve of the beam test sample is shown in figure 7.18.

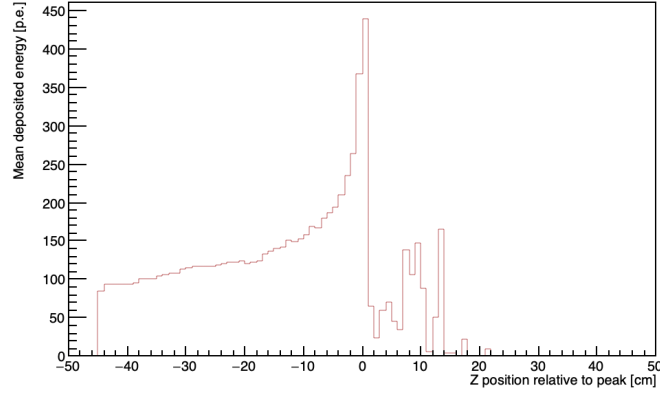


Figure 7.18.: The total dE/dz curve for the selected sample of beam test events.

The same procedure was used to construct the dE/dz curve of the selected 750 MeV/c simulation, the resulting curve is shown in figure 7.19.

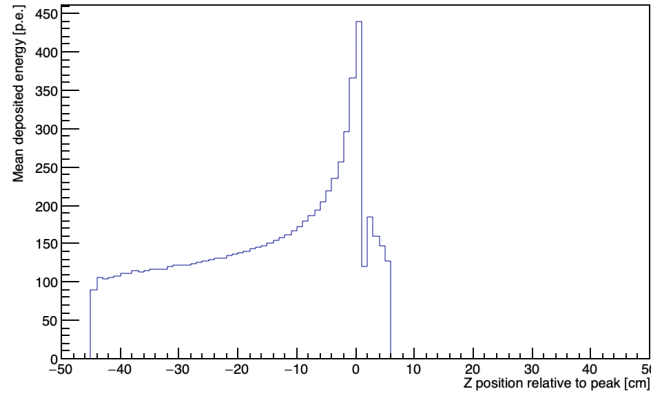


Figure 7.19.: The total dE/dz curve for the selected sample of simulation events.

7.5.2. dE/dz Comparison

In order to directly compare the dE/dz curves of the beam test data and the simulation, the dE/dz curves of the two samples were superimposed. Figure 7.20 shows the two superimposed curves along with the ratio plot between the two.

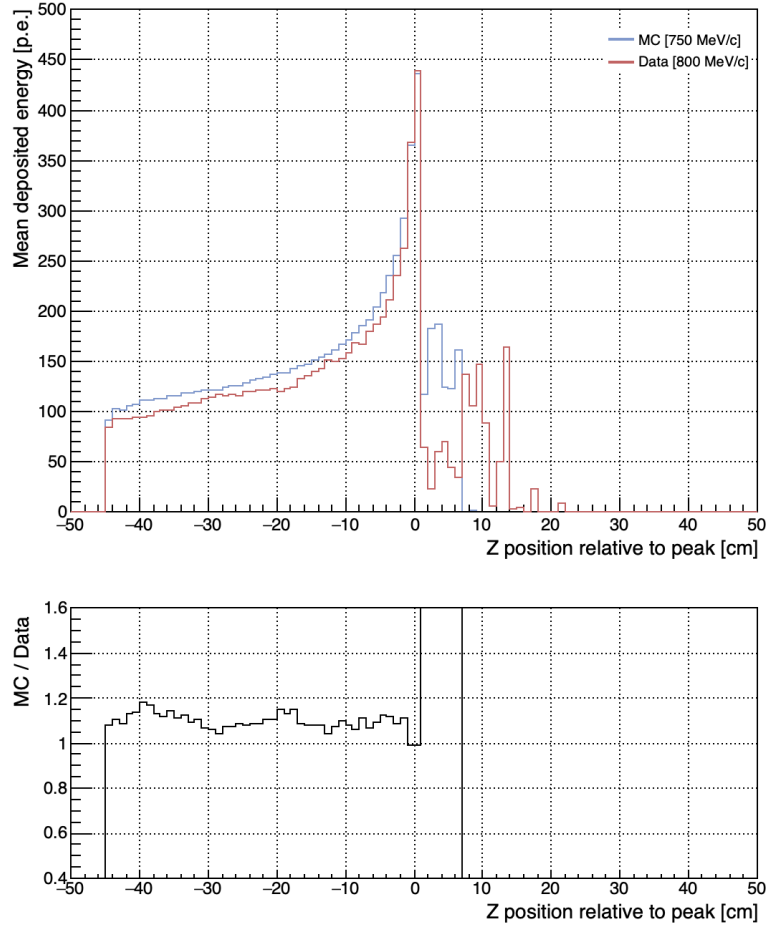


Figure 7.20.: dE/dz curves for a 750 MeV/c simulation and the beam test data and the ratio plot between the two.

According to figure 7.20, the dE/dz curves of the simulation and the beam test data are in reasonable agreement. They both display a plateau region with mean energy deposition of around 100 p.e. at the beginning and middle of the proton track, followed by a large energy deposition of around 450 p.e. towards the end of the track where the proton is expected to stop. In both cases there is a distribution of non-zero energy deposition beyond the expected stopping point.

To perform a more thorough comparison between the samples, the dE/dz curve is considered in three separate regions; the plateau region in the beginning and middle of the proton track, the peak region at the stopping point of the proton, and the region beyond the peak.

1. The Plateau Region

According to the ratio plot in figure 7.20, the energy deposition in the plateau region of the beam test sample is around 10% lower than that of the simulation.

As mentioned in section 6.2, the conversion of energy from units of MeV to units of photoelectrons, in the simulation of the detector response, is performed using measurements from the current FGD. It is known that this conversion factor requires further calibration for more accurate results. Therefore, it is very likely to be the cause of this discrepancy.

Since the simulation of the detector response is still at its early stages, there may also be some sources of energy losses and inefficiencies that affect the data but are not yet accounted for in the simulation. Examples of such effects include the fiber collection efficiency, the MPPC geometrical effects and the electronics response.

2. The Stopping Point Region

Figure 7.20 shows very good agreement between the beam test sample and the simulation at the stopping point of the proton. However, due to the discrepancy observed in the plateau region, there is a good chance that this agreement is only coincidental.

Assuming that the deviation between the curves is the result of the mis-calibration of the energy in the simulation, the dE/dz curve of the MC sample is re-calibrated with a 10% decrease in the energy deposition. Figure 7.21 shows the dE/dz curve comparison after performing the re-calibration, where a better agreement in the plateau region is observed.

According to the curves in figure 7.21, the energy deposition at the stopping point of the proton in the case of the beam test sample is higher than that of the simulation's by 16%. This discrepancy does not come as a surprise since the amount of light yield at the stopping point is heavily influenced by quenching effects. Although the simulation of the detector response includes a calculation of Birk's saturation, the value of Birk's constant used in these calculations is obtained from the SciBooNE experiment[¶] since the value of Birk's constant for the SuperFGD cubes is yet to be determined. Therefore, further studies into quenching in the SuperFGD may produce results that can improve the simulation of these effects.

[¶]SciBar Booster Neutrino Experiment, a neutrino experiment that was located at the Fermi National Accelerator Laboratory (Fermilab), which had a similar material to the SuperFGD cubes, but had a different production method.

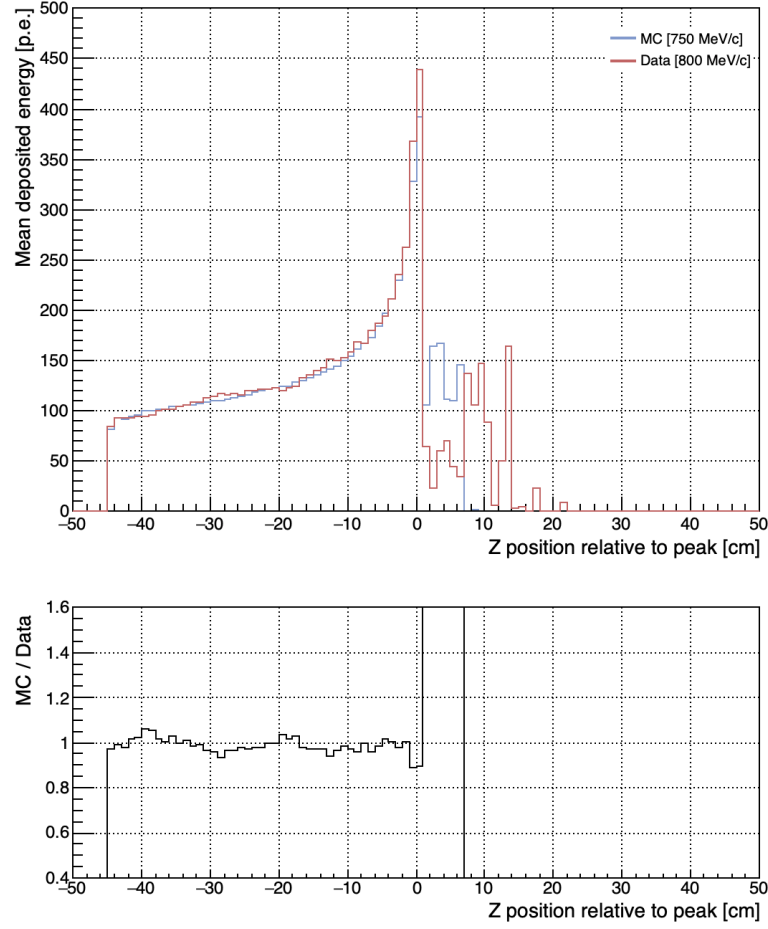


Figure 7.21.: dE/dz curves for a 750 MeV/c simulation and the beam test data and the ratio plot between the two after re-calibrating the simulation.

3. The Region Beyond the Peak

A small distribution is observed beyond the peak of the stopping point. This distribution is most likely due to interactions at the end of the track that cause scatterings or release secondaries. It is worth taking into consideration that due to the normalization used for the total dE/dz curve, this distribution may be caused by a very small number of events that exhibit such behaviour. In order to confirm that, figure 7.22 shows the percentage of events that occupy each Z position with respect to the total stopping proton events in the samples.

As seen in figure 7.22 (a), the first layer beyond the stopping point is almost always occupied and the second layer is occupied around 40% of the times. These two layers are most likely occupied by the expected crosstalk around the stopping point. On the other hand, the occupancy decreases significantly to about 7% for the third layer after the peak and less than 2% afterwards.

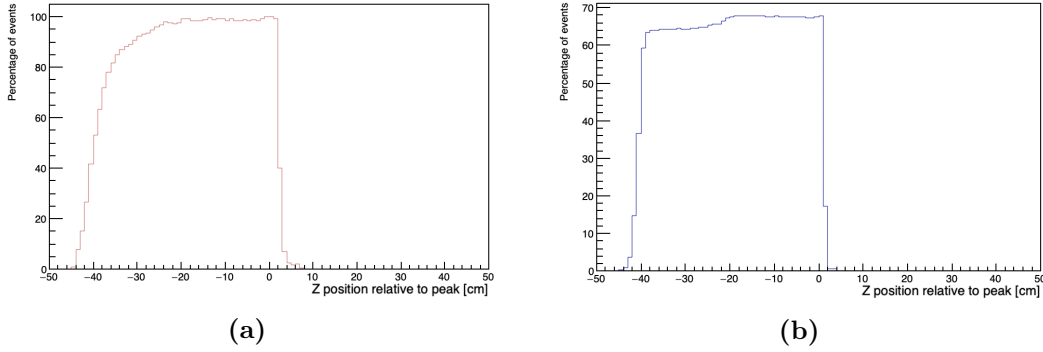


Figure 7.22.: The percentage of events that occupy each Z layer for the beam test sample (a) and the simulation sample (b).

In the case of the simulation, since no crosstalk was simulated, the next layer after the stopping point is occupied only in about 17% of the events. All layers after that have very low occupancy of less than 1%.

According to these results, it is evident that the distribution beyond the stopping point in the dE/dz curves is caused by a very small number of events that have passed the selection criteria. Figure 7.23 shows an event display of a beam test event where the proton has scattered downwards at the end of its track causing a relatively large energy deposition up to 6 cm beyond the cube with the maximum energy deposition.

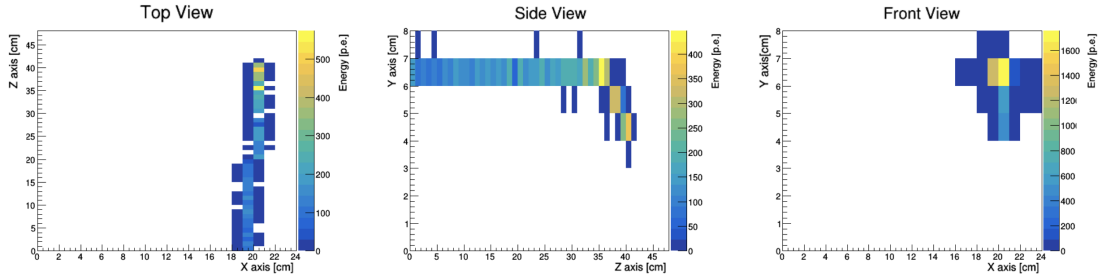


Figure 7.23.: An event display from the beam test data showing a proton scattering downwards at the end of the track.

Similarly for the simulation, figure 7.24 shows an event display of a 750 MeV/c proton that undergoes an interaction towards the end of its track, contributing to that distribution.

Due to the low statistics in this region, it is very difficult to draw any conclusions on interaction at the end of the proton tracks. A larger percentage of these interactions may be possible to obtain by modifying the event selection criteria. More specifically, the condition on the the spread in the front (XY) view (cut number 3).

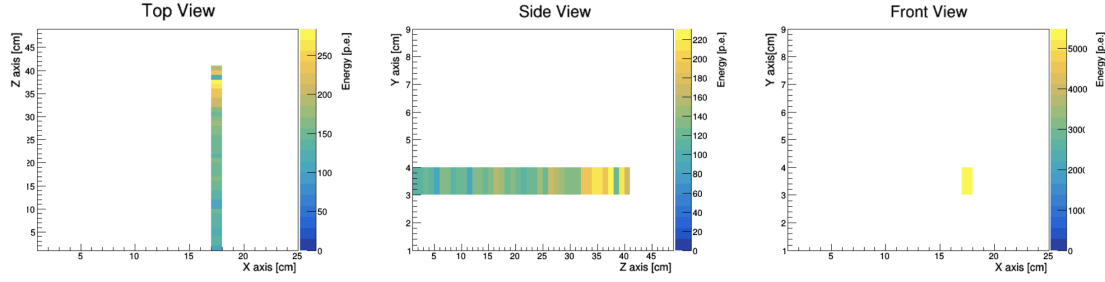


Figure 7.24.: An event display from the 750 MeV/c simulation showing a proton interacting at the end of the track.

7.5.3. Fiber Response Comparison

The comparison between the beam test data and the simulations can be extended to perform some fiber response comparisons between the two samples. The attenuation observed in the beam test data can be used to verify the simulation of attenuation in the MC. Furthermore, the amount of energy collected by two orthogonal fibers for the same hit can be compared and used to investigate any sources of non-uniformity in the fiber response.

7.5.3.1. Attenuation

The effect of the attenuation of light as it travels along the fibers can be seen by comparing the total energy recorded by the horizontal fibers with the energy recorded by the vertical ones. Due to the difference in their lengths, the longer horizontal fibers (24 cm) are expected to suffer from more attenuation compared to the shorter vertical ones (8 cm). Figure 7.25 shows the ratio between the two.

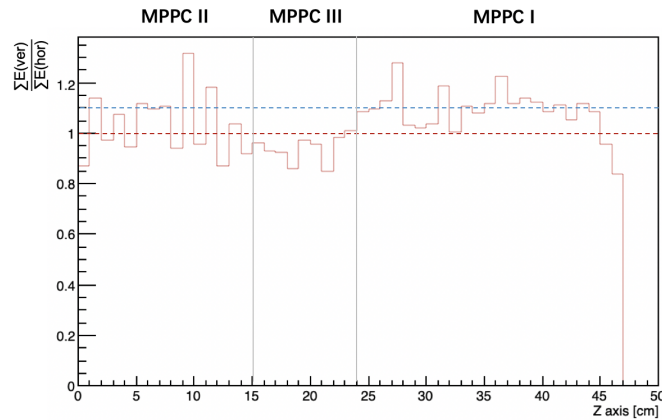


Figure 7.25.: The ratio between the total energy deposited in the vertical fibers and the total energy deposited in the horizontal fibers as a function of the Z axis for the beam test sample. The MPPC type for the vertical fibers is shown at the top of the plot, while all horizontal fibers are equipped with MPPC type I.

Due to the fact that the vertical fibers are connected to three different types of MPPCs, the comparison between the two is only valid in the region towards the end of the detector where MPPCs of type 1 were used for both vertical and horizontal fibers. In this region, the ratio of the total energy recorded by the vertical fibers to the total energy recorded by the horizontal ones is around 1.1, showing a 10% larger signal in the vertical fibers compared to the horizontal ones.

In the case of the simulations, the attenuation is introduced to the energy using equation 6.2. To verify that the attenuation in the MC is in agreement with the attenuation observed in the data, the same ratio is plotted in figure 7.26.

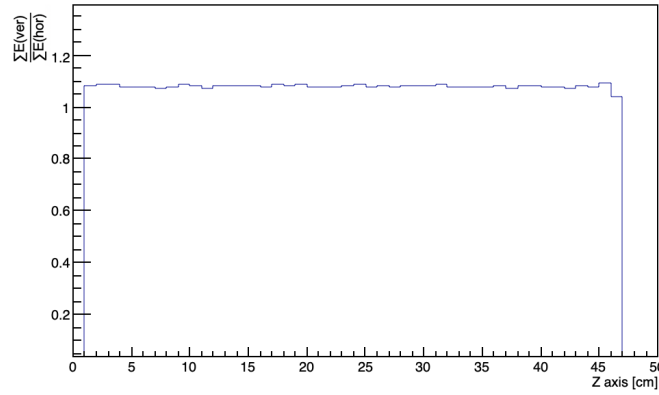


Figure 7.26.: The ratio between the total energy deposited in the vertical fibers and the total energy deposited in the horizontal fibers as a function of the Z axis for the simulation sample.

According to figure 7.26, the MC also shows an excess of about 10% in the energy recorded by the vertical fibers compared to the horizontal ones. Since the simulations do not account for the different types of MPPCs, this ratio is observed across the whole detector.

7.5.3.2. Energy Deposition

Each cube of the SuperFGD is read out by three orthogonal fibers along the three axes (X, Y and Z). In the case of the beam test, as well as in the simulations, the beam was along the Z axis which causes a large amount of energy to be read out by the fibers along this direction. This makes it very difficult to distinguish between separate hits in these fibers, it may also lead to the saturation of the MPPCs connected to them. Because of this limitation, only the XZ and ZY views are used in the analysis.

The stopping point of the proton can be used to compare the amount of energy recorded by the vertical and the horizontal fibers. Ideally, the two fibers are expected to see the same amount of energy with some variation caused by the attenuation.

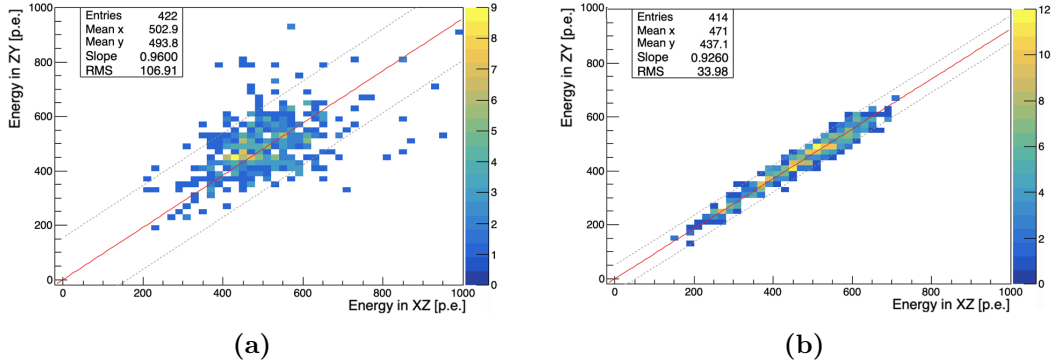


Figure 7.27.: The energy recorded by two orthogonal fibers at the proton stopping point for the beam test sample (a) and the simulation sample (b). The dashed lines show the RMS of the sample with respect to the fit line.

Figure 7.27 shows a 2D plot of the energy recorded by the horizontal fibers versus the energy recorded by the vertical ones at the stopping point of the proton for both samples. To make sure that the same type of MPPC detects both signals, only events with ranges larger than 24 cm are considered from the beam test sample.

Figure 7.27 shows a clear difference between the beam test sample and the simulation. In the case of the simulation, the points are localized in a line with minimum variation between the two fibers and an RMS (Root mean square) of 33.98 p.e. On the other hand, the beam test data shows much larger variation between the energies recorded by the two orthogonal fibers for the same hit. The RMS of the beam test sample is calculated to be 106.91 p.e., which is over 3 times that of the simulation's.

The presence of hits with energies up to 1000 p.e. hints at a calibration issue. As explained in section 4.6.5., three signal paths are used to create the hit amplitude used in the analysis (hit charge). These are the high gain (HG), low gain (LG) and Time-over-Threshold (ToT) signals. The source of the amplitude for each hit in figure 7.27 (a) is extracted and a summary of the number of hits for each signal path is shown in table 7.7.

Table 7.7.: The origin of the amplitudes in figure 7.27 (a).

View	Signal Path	Number of Hits
XZ	HG signal	0
	LG signal	254
	ToT signal	168
ZY	HG signal	0
	LG signal	264
	ToT signal	158

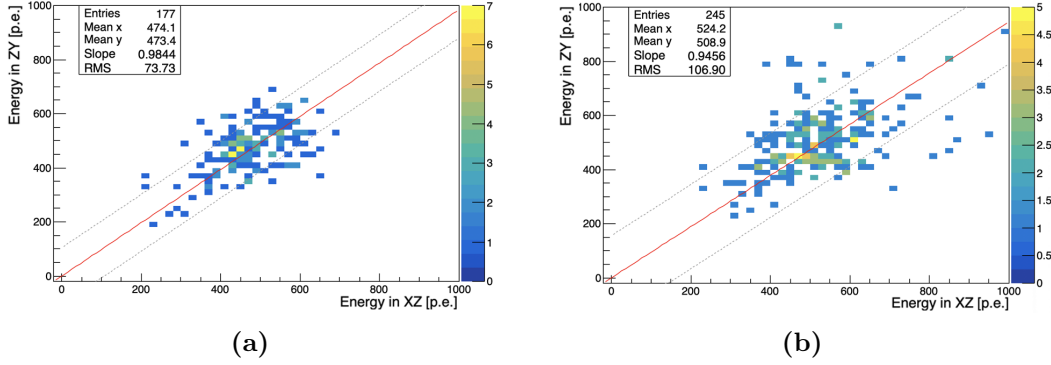


Figure 7.28.: The energy recorded by two orthogonal fibers at the proton stopping point for the beam test sample. Figure (a) shows hits with an amplitude originating from a LG signal in both fibers, while figure (b) shows the distribution when one of the fibers has a hit from a ToT signal.

The energy deposition at the stopping point of the proton is beyond the saturation limit of the HG signal (~ 125 p.e.) which explains the absence of HG signals in table 7.7. On the other hand, LG signals do not saturate until around 800 p.e. making them the main source of amplitude for hits at the stopping point.

While the HG and LG signals are well calibrated, the calibration of the ToT signal is less accurate for high energy signals. The effect of the calibration on the distribution in figure 7.27 (a) can be clearly observed by separating the LG hits from the ToT hits, as shown in figure 7.28.

From figure 7.28, it is clear that the large spread of the points at high energy (over 700 p.e.) is partly a result of the inefficiency of the ToT calibration. By eliminating the ToT hits, the RMS of the beam test sample was reduced by 30% to a value of 73.73 p.e. This raises the need for a better treatment of the ToT calibration at these energies.

When considering only LG hits, the variation is significantly lower. However, it is still more than twice of what is observed in the simulation. This spread can be a consequence of several effects that are missing in the simulation, such as the non-uniformity of light yield in a cube or the difference in the recorded energy between the two fibers based on the location of the hit within the cube and its proximity to each fiber.

Another factor to take into consideration is that the conditions of the SuperFGD prototype are not as ideal as the simulation's, which may introduce some non-uniformities in the responses of the different elements like the cubes, fibers and MPPCs. All of these effects are subjects of ongoing studies that are yet to be published.

7.6. Effect of Cube Coating, Holes and Fibers(From Simulations)

As described in chapter 6, the cube coating in the simulations of the SuperFGD is considered a dead volume such that any energy deposited in the coating layers will not be stored in the output.

To quantify the contribution to missing energy of a cube coating of 0.1 mm thickness, the ratio between the coating volume and the total cube volume can be used.

$$\frac{10 \times 10 \times 10 \text{ mm}^3 - 9.8 \times 9.8 \times 9.8 \text{ mm}^3}{10 \times 10 \times 10 \text{ mm}^3} \times 100\% = 5.88\% \quad (7.7)$$

Therefore, the dead volume introduced by the cube coating constitutes around 6% of the cube volume. In order to investigate the extent of its effect, two sets of simulations were used; one with coating and one without. Two beam momentum values were selected for this comparison, 700 MeV/c and 750 MeV/c.

Figure 7.29 shows the total energy deposited in the horizontal fibers for each stopping proton event, for both momenta and both coating conditions. According to this figure, the mean total deposited energy increases by 4.2% (for the 750MeV/c sample) and 2.8% (for the 700MeV/c sample) when no coating is simulated.

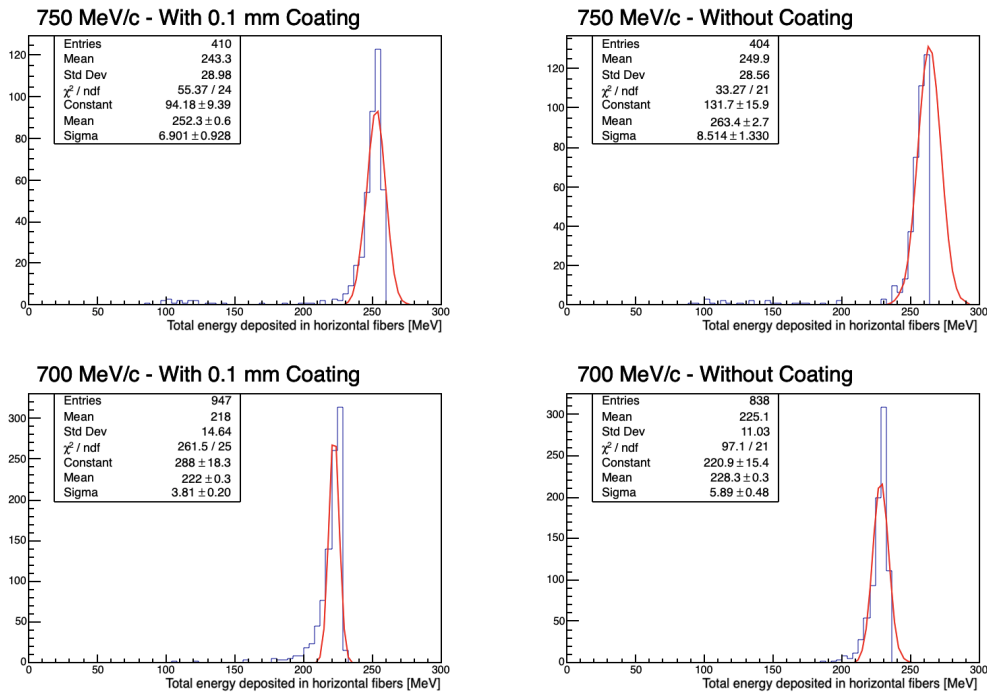


Figure 7.29.: Total energy deposited in the horizontal fibers, comparison between two samples with cube coating and two samples without.

To eliminate all sources of dead volume in the detector, two additional simulations were created with beam momenta of 700 and 750 MeV/c. In these simulations, neither the cube coating nor the holes or fibers were simulated. Figure 7.30 shows the comparison between the two new simulations and the regular simulations with the fibers and cube coating.

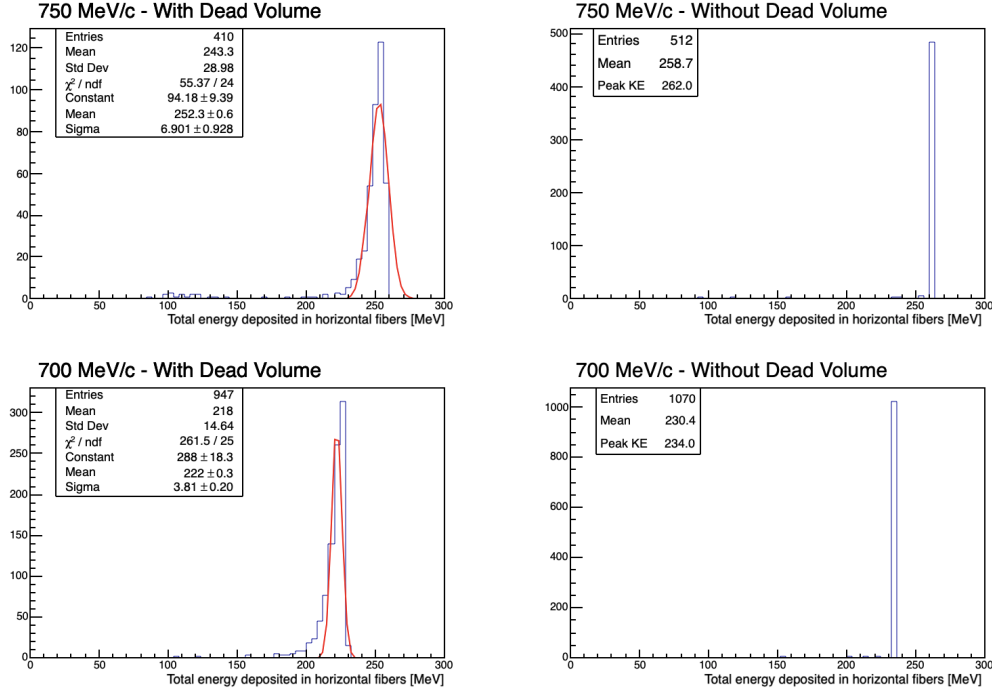


Figure 7.30.: Total energy deposited in the horizontal fibers, comparison between two samples with holes and fibers (and cube coating) and two samples without any dead volume.

Evidently, when no sources of dead volume are present in the simulations, the total energy is a sharp localized peak at the energy value corresponding to the beam momentum. In the case of the 750 MeV/c simulation, the peak is located at an energy of 262 MeV. For the 700 MeV/c simulation, the peak position is at 234 MeV. These results provide an explanation for the discrepancy between the true and reconstructed beam momenta of the simulations, observed in section 7.4.2.

The contribution of the fibers to the missing energy can be quantified by comparing their volume to the volume of a cube as follows:

$$\frac{0.5^2 \times \pi \times 10 \text{ mm}^3}{10 \times 10 \times 10 \text{ mm}^3} \times 100\% = 0.79\% \quad (7.8)$$

With the cube coating, the total percentage of dead volume in one cube of the SuperFGD in the simulations is 6.67%.

Finally, the range of the protons is revisited after the removal of the holes. Figure 7.31 shows a comparison between the range of two samples with the cube coating, holes and fibers and two samples without them.

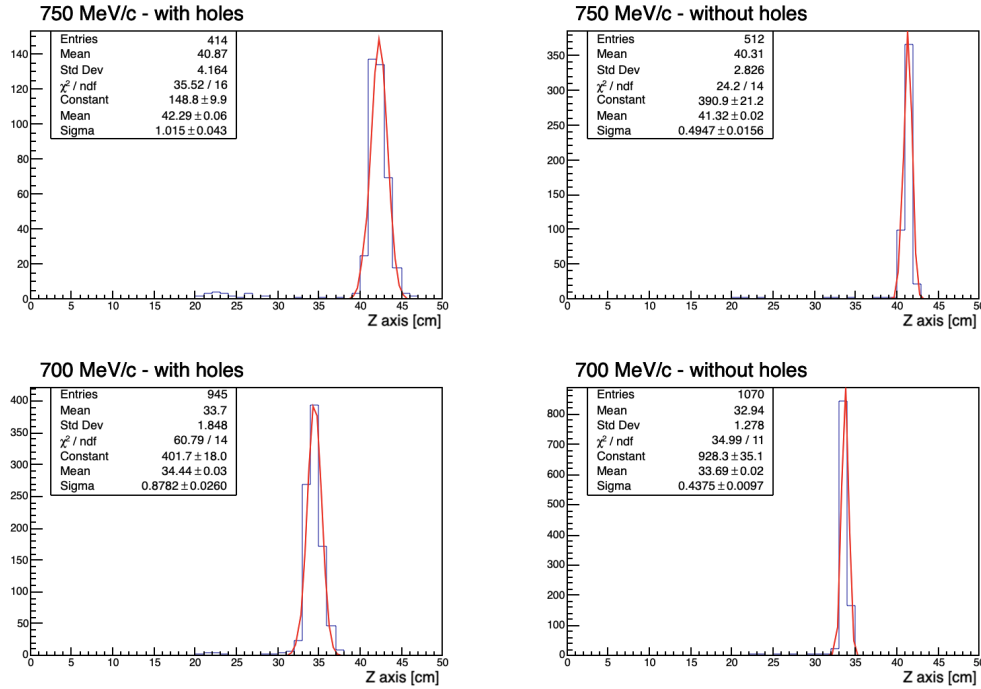


Figure 7.31.: The range of protons in the SuperFGD, comparison between two samples with holes and fibers (and cube coating) and two samples without any dead volume.

Since the densities of the materials used for the coating and the fibers are similar to the density of the cube material, excluding the coating and the fibers from the simulation is not expected to have a direct effect on the range. On the other hand, a slight effect on the range may arise when considering that protons may travel through the air between the hole and the fiber. This effect may be observed in figure 7.31 by the slight reduction of the proton range when the holes are not included in the simulation. This can also explain the lower sigma, since the cubes in these simulations are of the full $10 \times 10 \times 10 \text{ mm}^3$ volume with no variation, which causes a uniform behaviour for the protons in the sample.

*I do not want to believe,
I want to know.*

— Carl Sagan

8

Conclusion

The goal of this study was to use stopping protons as a tool to analyze the beam test data of the SuperFGD prototype, as well as to examine the SuperFGD simulations and their agreement with the data. One simulation was selected from 5 samples based on its similarity to the beam test sample with respect to the range of the protons and their initial momentum. This sample was used to perform a comparison with the test data.

The dE/dx curves for both samples were extracted and compared. Apart from a 10% deviation, likely caused by a mis-calibration of the energy in the simulation, beam test data and simulations exhibit a similar behaviour of a steady energy deposition along the majority of the proton track, followed by a steep increase at the proton's stopping point. Some energy deposition was observed beyond the peak, which can be the starting point for investigating nuclear interactions at the stopping point of the proton.

A comparison between the fiber attenuation observed in the data and the simulation shows a consistent 10% decrease in the light yield recorded by the horizontal fibers compared to the vertical ones in both samples. This result illustrates a good approximation of the attenuation in the simulation of the detector response. When comparing the energy recorded by two orthogonal fibers for the same cube, the simulation shows minimum variation between the two fibers with an RMS of 33.98 p.e., while the data sample has a large spread with an RMS of 106.91 p.e. When eliminating the effect of the inefficiency of the ToT calibration at high energies, the RMS is reduced by 30%.

This study highlights the impact of the absence of some effects in the current SuperFGD simulations. The ND280 upgrade simulation is a work in progress that is at a stage of rapid improvements. As this study was ongoing, several updates were performed and some of which were the results of this work.

Bibliography

- [1] The T2K Collaboration, *The T2K Experiment*, NIM A, Volume 659, p106-135, 2011
- [2] Blondel, A et al., *The T2K-ND280 upgrade proposal*, CERN-SPSC-2018-001
- [3] The T2K Collaboration, *T2K ND280 Upgrade - Technical Design Report*, January 15, 2019.
- [4] The T2K Collaboration, *The T2K Fine-Grained Detectors*, 16 Apr 2012.
- [5] J.A. Formaggio and G.P. Zeller., *From eV to EeV: Neutrino Cross Sections Across Energy Scales*, Rev. Mod. Phys. 84 (2012) 1307.
- [6] Dean Karlen, on behalf of the T2K Collaboration, *Latest Results from the T2K Neutrino Experiment*, January 2019, DOI: 10.3390/universe5010021
- [7] Birks, J.B., *Scintillations from Organic Crystals: Specific Fluorescence and Relative Response to Different Radiations*, 1951 Proc. Phys. Soc. A 64 874
- [8] Birks, J.B., *The Theory and Practice of Scintillation Counting*, London: Pergamon (1964)
- [9] L. Verhey, H. Blattman, P. M. Deluca, D. Miller, *Proton Interactions with Matter*, Journal of the ICRU, Volume os30 (2) – Dec 15, 1998
- [10] M. Tanabashi et al., *Particle Data Group*, Phys. Rev. D 98, 030001 (2018).
- [11] T2K Collaboration (Kudenko, Yury for the collaboration), *The Near neutrino detector for the T2K experiment*, Nucl.Instrum.Meth. A598 (2009) 289-295.
- [12] Claudio Giganti, Marco Zito, *Particle Identification with the T2K TPC*, October 2009.
- [13] Y. Giomataris, Ph. Rebourgeard, J.P. Robert and G. Charpak, *MICROMEGAS: a high-granularity position-sensitive gaseous detector for high particle-flux environments*, Nucl. Instr. Meth. A376(1996)29-35
- [14] Review of Particle Physics, Phys. Lett. B 667 (2008) 1
- [15] Glenn F. Knoll, *Radiation Detection and Measurement*, Wiley, 1989.

-
- [16] Leo, William R., *Techniques for Nuclear and Particle Physics Experiments*, Springer, 1994.
- [17] Kuraray WLS Fibers. , <http://kuraraypsf.jp/psf/ws.html>
- [18] Oleg Mineev, INR RAS, Moscow, Nov. 13, 2018.
- [19] A. Ghassemi, K. Sato, K. Kobayashi, *Technical Note/MPPC*, Hamamatsu.
- [20] Hamamatsu, *MPPC S13360-1325PE Data Sheet*, Aug, 2016.
- [21] Chen Xu (Dissertation), *Study of the Silicon Photomultipliers and Their Applications in Positron Emission Tomography*, Universität Hamburg, 2014.
- [22] Katsushige Kotera, Weonseok Choi, Tohru Takeshita, *Describing the response of saturated SiPMs*, Shinshu University, 2016.
- [23] E. Noah et al., *Readout scheme for the Baby-MIND detector*, PoS PhotoDet2015 (2016) 031.
- [24] East Area Documentation, <http://sba.web.cern.ch/sba/BeamsAndAreas/East/East.htm>
- [25] L. Durieu, O. Ferrando., *Design of T9 (Atlas/CMS) for EHNL*, PS/PA 96-39, CERN, 1996.
- [26] The North Target, <http://sba.web.cern.ch/sba/targets/TargetNorth.html>
- [27] Lau Gatignon, *The T9 Beam*, 10 March, 2014.
- [28] Proton Stopping-Power and Range (PSTAR), National Institute of Standards and Technology (NIST), <https://physics.nist.gov/PhysRefData/Star/Text/PSTAR.html>
- [29] Rene Brun and Fons Rademakers, *ROOT - An Object Oriented Data Analysis Framework*, Proceedings AIHENP'96 Workshop, Lausanne, Sep. 1996, Nucl. Inst. Meth. in Phys. Res. A 389 (1997) 81-86. See also <http://root.cern.ch/>
- [30] Mohr, P.J.; Taylor, B.N. and Newell, D.B. (2015), *The 2014 CODATA Recommended Values of the Fundamental Physical Constants*, National Institute of Standards and Technology, Gaithersburg, MD, US.



Calculation of Uncertainties

A.1. Uncertainty in the Reconstructed Momentum

The uncertainty in the value of the reconstructed beam momentum was calculated using error propagation. For a function $f(x, y)$ the uncertainty σ_f is related to the uncertainties σ_x and σ_y (Provided that σ_x and σ_y are uncorrelated) by:

$$\sigma_f^2 = \left(\frac{\delta f(x, y)}{\delta x} \right)^2 \sigma_x^2 + \left(\frac{\delta f(x, y)}{\delta y} \right)^2 \sigma_y^2 \quad (\text{A.1})$$

The proton beam momentum, as a function of its mass and kinetic energy, is given by:

$$p = \sqrt{(KE + m)^2 - m^2} \quad (\text{A.2})$$

The corresponding uncertainty in the momentum, according to error propagation, is given by:

$$\sigma_P = \sqrt{\left(\frac{KE + m}{\sqrt{(KE + m)^2 - m^2}} \right)^2 \sigma_{KE}^2 + \left(\frac{KE}{\sqrt{(KE + m)^2 - m^2}} \right)^2 \sigma_m^2} \quad (\text{A.3})$$

Using the uncertainty in the mass of the proton (0.00000029 MeV)^[30], this formula is used in the analysis to calculate the uncertainty in the momentum for each sample.

A.2. Uncertainty in the Kinetic Energy From The Range

In section 7.5, the kinetic energy as a function of the range was described by:

$$KE(x) = 74.25 + 4.925x - 0.01572x^2 \quad (\text{A.4})$$

According to the propagation of errors, the uncertainty in the kinetic energy can be calculated from the uncertainty in the range using the relation:

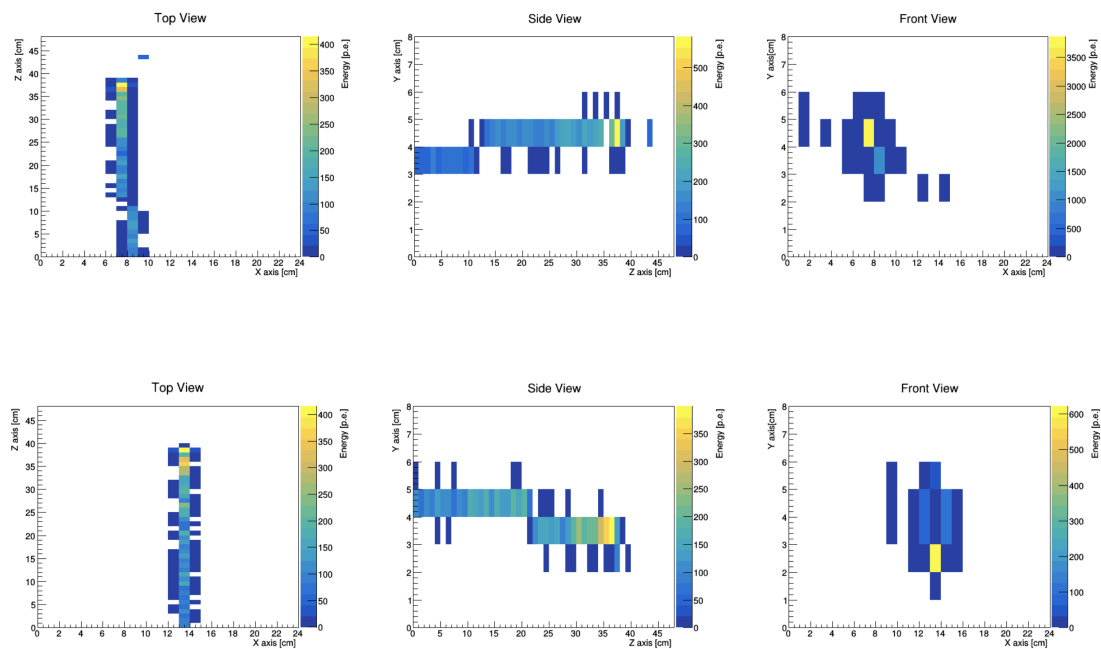
$$\sigma_{KE} = (4.925 - 2 \times 0.01572)\sigma_x \tag{A.5}$$

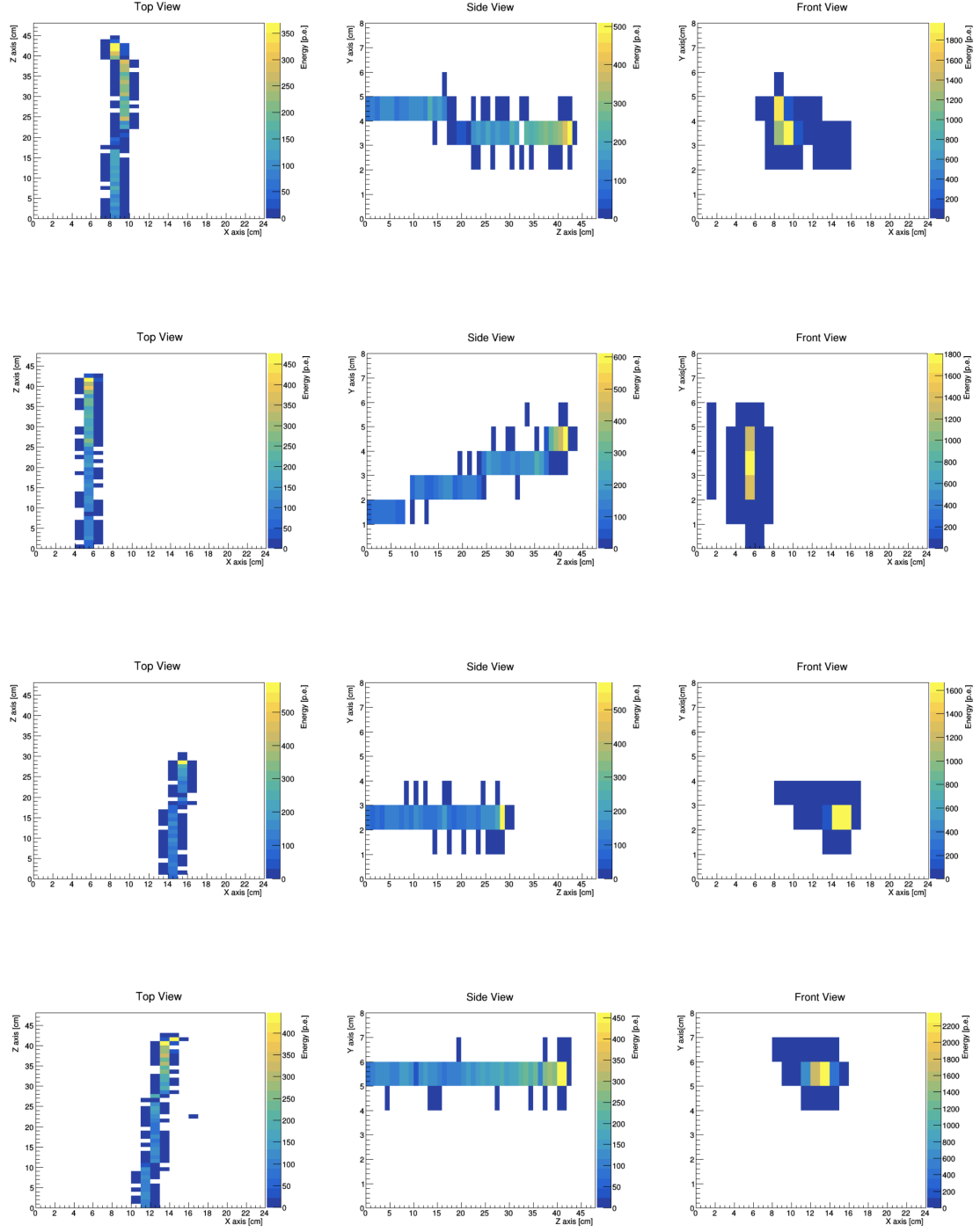
B

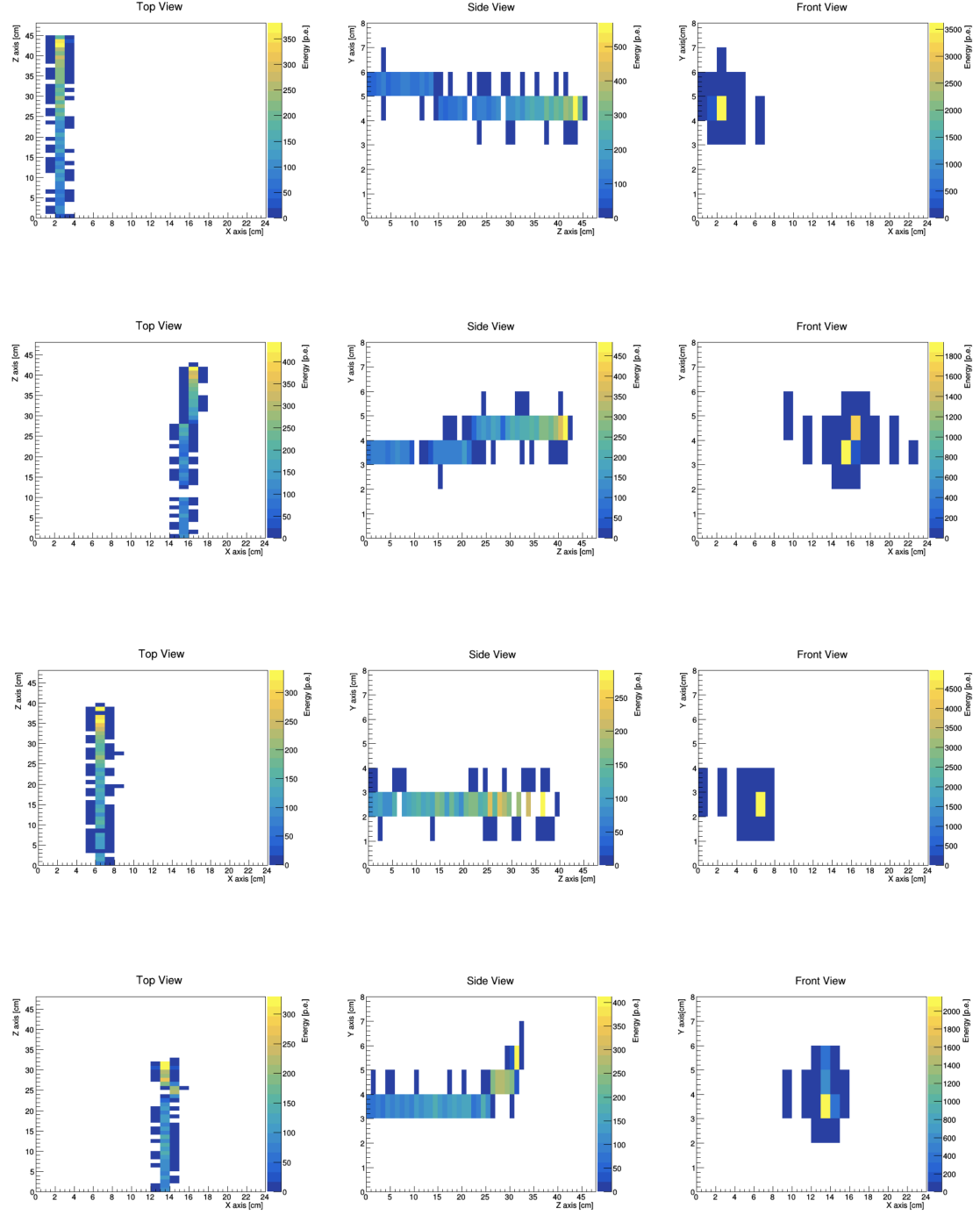
Samples of Event Displays

B.1. 800 MeV/c Beam Test Sample

A random sample of stopping proton event displays is shown below for reference.







B.2. 750 MeV/c Simulation Sample

A random sample of stopping proton event displays is shown below for reference.

